Electronic Supplementary Information

Halozincate Ionic Liquid Electrolyte Enabled High-Temperature Dendrite-free Zn Metal Batteries

Mingchen Yang,[a] Xiuyang Zou,[b] Mingzhu Wu,[a] Jiangtao Yu,[a] Xinyu Ma,[a] Yin Hu[a,*] and Feng Yan [a,*]

[a] Jiangsu Engineering Laboratory of Novel Functional Polymeric Materials, Jiangsu Key Laboratory of Advanced Negative Carbon Technologies College of Chemistry, Suzhou Key Laboratory of Soft Material and New Energy, College of Chemistry, Chemical Engineering and Materials Science, Soochow University, Suzhou 215123, China.
E-mail: yinhu045@suda.edu.cn; or fyan@suda.edu.cn

[b]Jiangsu Engineering Research Center for Environmental Functional Materials, School of Chemistry and Chemical Engineering, Huaiyin Normal University, Huaian, 223300, China.

Experimental Procedures

Materials

1-Methylimidazole, 1-chlorohexane, bromoethane, zinc chloride ($ZnCl_2$; ≥99%), N-methyl-2-pyrrolidone (NMP, 99.9% purity), dimethyl sulfoxide-d6 (DMSO-d6, 99.9% purity), ether, and ethyl acetate were purchased from Sigma-Aldrich. Zinc foil (10 μm), titanium foil (10 μm), and the NVP, PVDF binder with an average M_W of ~534,000, Super P (99.5% purity), glass fiber separator (Whatman GF/D) were purchased from Shenzhen kejing star technology company. All chemical reagents were employed without further purification. Deionized water was used throughout the experiment.

Synthesis of Imidazolium-Type ILs

[HMIM]Cl was synthesized as follows: A mixture containing 1-methylimidazole (10.34 g, 0.11 mol) and 1-chlorohexane (12.1 g, 0.10 mol) was stirred at 80 °C for 3 days. The products were washed with ethyl acetate and ether 3 times, then dried for 24 h under a dynamic vacuum at 60 °C. ^{1}H NMR (400 MHz, DMSO-d6): δ=9.33 (s, 1H), 7.82 (s, 1H), 7.74 (s, 1H), 4.17 (t, 2H), 3.86 (s, 3H), 1.76 (m, 2H), 1.24 (m, 2H), 0.85 (t, 3H) (**Fig. S1A**).

$[HMIM]_2[ZnCl_4]$ was synthesized via the stirring of [HMIM]Cl with anhydrous $ZnCl_2$ at 50 °C for 8 h until a homogeneous and transparent target liquid was obtained. ^{1}H NMR (400 MHz, DMSO-d6): δ=9.18 (s, 1H), 7.78 (s, 1H), 7.71 (s, 1H), 4.17 (t, 2H), 3.86 (s, 3H), 1.76 (m, 2H), 1.24 (m, 2H), 0.85 (t, 3H) (**Fig. S1B**).

[EMIM][TFSI] was synthesized as follows: A mixture containing 1-methylimidazole (10.34 g, 0.11 mol) and bromoethane (10.89 g, 0.10 mol) was stirred at 25 °C for 24 h. The products 1-Ethyl-3-methylimidazolium bromide ([EMIM]Br) were washed with ethyl acetate and ether 3 times, then dried for 24 h under a dynamic vacuum at 60 °C. The ionic liquid was mixed with an equal molar amount of LiTFSI. The obtained solution was stirred for anion exchange at room temperature for 4 h. The mixture was washed three times with deionized water and dried under vacuum at 60 °C. ^{1}H NMR (400 MHz, DMSO-d6): δ=9.09 (s, 1H), 7.77 (s, 1H), 7.68 (s,1H), 4.17 (t, 2H), 3.83 (s, 3H), 1.40 (t, 3H) (**Fig. S3**).

Preparation of halozincate ionic liquid electrolytes

The HZLE-1 consists of $[HMIM]_2[ZnCl_4]$, $ZnCl_2$, and [EMIM][TFSI] in a molar ratio of 1:2:1, while HZLE-0.5 and HZLE-2 have molar ratios of 1:2:2 and 2:4:1 for their components, respectively.

Preparation of electrodes

To prepare the NVP slurry, a mixture consisting of 75 wt% $Na_3V_2(PO_4)_3$ as the active material, 15 wt% Super P as a conductive agent, and 10 wt% polyvinylidene fluoride (PVDF) as the binder in NMP solvent was stirred overnight to achieve a homogeneous slurry. Subsequently, the cathode slurry was cast onto titanium foil using a standard doctor-blade technique, followed by drying at 80 °C overnight in an oven.

Characterization

^1H NMR spectra of the synthesized ILs were obtained with a Bruker Avance (400 MHz) spectrometer in DMSO-d6. FT-IR spectra of ILs were recorded with an IR Tracer-100 over a range of 600-4000 cm^{-1}. Viscosities of the electrolytes were analyzed with a rheometer (MCR 702 TwinDrive) via scanning a temperature from 25 to 120 °C. TGA was conducted with a Perkin Elmer 4000 in a nitrogen atmosphere with a heating rate of 5 °C min^{-1}. The morphology and element analyses of the samples were examined by SEM (Hitachi Regulus 8230, Japan) equipped with an EDS attachment and AFM (Bruker Multimode8, USA). XRD was performed on a Bruker D8 VENTURE X-ray diffractometer (50 kV, 1 mA) using Cu Kα radiation (λ = 1.5418 Å). Raman and in-situ Raman spectra were obtained using a confocal micro-Raman system (XploRA PLUS, Jobin Yvon, France). All experiments were carried out at an excitation line of 638 nm from an internal He-Ne laser with a power of 8.37 mW. The metal ions concentrations in the electrolytes were investigated using a PerkinElmer Optima 5110 ICP-OES system. The electrolytes were diluted with an 8% aqueous solution of hydrochloric acid, and at least 5 ICP standard solutions were used to generate calibration curves, with correlation coefficients greater than 0.999. The wavelengths were used in the axial mode: sodium (589.592 nm), vanadium (292.401 nm), and zinc (213.857 nm). X-ray photoelectron spectroscopy (XPS) spectrum was obtained by using Thermo Scientific ESCALAB Xi+ and the characteristic

spectra of electrodes at different depths were probed by sputtering the electrodes with Ar^+ at different times.

Electrochemical measurements

The NVP cathode is coated on Ti foil with an active mass loading of 9 mg cm^{-2} for both CR2032 coin and pouch cells. Zn metal foil with thicknesses of 10 μm was used as an anode for both CR2032 coin and pouch cells. The Zn foil and NVP cathode were punched in a diameter of 16 mm for the CR2032 coin cell and 4 cm* 5 cm (width * length) for the pouch cell tests. The CR2032 coin and pouch cells were assembled using Whatman glass fiber as separator (Whatman GF/D). The N:P ratio of the coin cells and pouch cells is 2. All batteries were assembled in an argon-filled glove box with water and oxygen content maintained at < 0.1 ppm. GCD data were collected using a LAND-CT2001A battery testing instrument at temperatures ranging from 25 to 120 °C. CV tests were conducted on a CHI760C electrochemical workstation. Electrochemical impedance spectroscopy (EIS) tests were performed on the CHI760C with an AC voltage of 10 mV amplitude in the frequency ranging from 10^5 Hz to 0.1 Hz at various temperatures from 20 to 120 °C.

Ionic conductivities were tested by two blocking electrodes (SS) and calculated according to the following Equation S1:

$$\sigma_i = \frac{L}{R \times S} \tag{S1}$$

where L and S represent the length between two electrodes and the area of the electrodes respectively. R is the resistance measured by EIS. The Zn ion transference number (t_{Zn}^{2+}) was tested following the method described by Abraham et al,[32] Zn|HZLE-1|Zn symmetric cells were assembled and polarization potential (ΔV) at 50 mV was applied. t_{Zn}^{2+} is estimated by the following Equation S2:

$$t_{Zn^{2+}} = \frac{I^{SS}(\Delta V - I^0 R_i^0)}{I^0(\Delta V - I^{SS} R_i^{SS})} \tag{S2}$$

Then the initial (I^0) and steady-state (I^{ss}) polarization current values were recorded. (**Fig. S8**). The initial and steady-state values of the bulk resistances (R_b^0 and R_b^{ss}) and electrode-electrolyte interfacial resistances (R_i^0 and R_i^{ss}) were examined using EIS before and after potentiostatic polarization. The first data point was recorded at 0.05 s.

Molecular dynamics simulations

MD simulations were performed to investigate the solvation structure of $ZnCl_2$-based electrolytes, together with the Zn conduction behavior under the electric field. All molecular dynamics simulations were performed using the Materials Studio software package. The force field used in simulation systems was COMPASSII, which assigned charges to all particles. Periodic boundary conditions were applied in the x, y, and z directions. For the long-range electrostatic interactions, the Ewald summation method was employed to achieve an accuracy of 0.0001 kcal mol^{-1}, while the van der Waals interactions were calculated using the Atom-based summation method with a cutoff distance of 12.5 Å. In this study, the molecular models of $[HMIM]_2[ZnCl_4]$, $ZnCl_2$, and [EMIM][TFSI] were built and optimized. Each system contained 300 $[HMIM]_2[ZnCl_4]$, 600 $ZnCl_2$, and 300 [EMIM][TFSI]. The system was simulated with an outside electric field and without an electric field, where the electric field strength was 1.4 V $Å^{-1}$ in Z directions. These systems were subjected to the steepest-descent energy minimization of 2000 steps, followed by five cycles of annealing and a 3 ns NPT equilibrium simulation (time step=1 fs, frame output for every 10000 steps, T=298 K). Then, the production NVT simulation was performed for 1 ns (time step=1 fs, frame output for every 5000 steps, T=298 K).

Recovery process of HZLE

After adding distilled water to HZLE-1, [HMIM]Cl remained dissolved in the water phase while [EMIM][TFSI] separated from the water due to its hydrophobicity. Consequently, Zn^{2+} in the IL hydrolyzed and precipitated as $Zn_4(OH)_8Cl_2 \cdot H_2O$ out of the water. As a result, [EMIM][TFSI] was separated and then subjected to rotary evaporation to obtain recycled [EMIM][TFSI]. At the meantime, the water-soluble [HMIM]Cl was recovered by dichloromethane extraction to remove the dissolved V and Na, and the dichloromethane was recycled by evaporation. The recovery rate is estimated by the following Equation S3:

$$Recovery\ rate = \frac{m_{recycled}}{m_{pristine}} \times 100\% \quad \text{(S3)}$$

where $m_{recycled}$ and $m_{pristine}$ are the mass of the recycled IL and initial raw material, respectively.

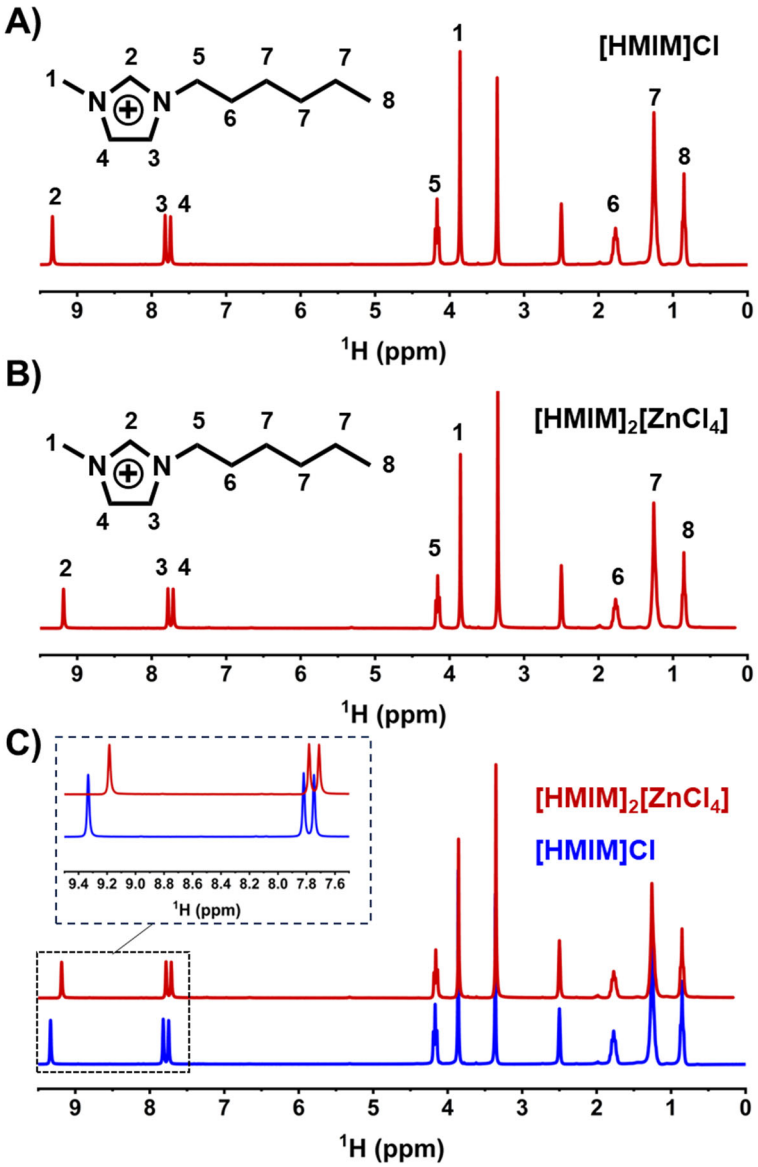

Fig. S1 ^{1}H NMR spectra of (A) [HMIM]Cl, (B) $[HMIM]_2[ZnCl_4]$, and (C) contrast magnification of C-H on the imidazolium cation, which indicates the effect of adding metal ions on the imidazolium cation. The characteristic peaks at 9.33 ppm, 7.82 ppm, and 7.74 ppm in the ^{1}H NMR spectrum are attributed to the active hydrogens (C-2, C-3, and C-4) on the imidazolium ring which shifts to 9.18 ppm, 7.78 ppm, 7.71 ppm due to the coordination of metal ions.

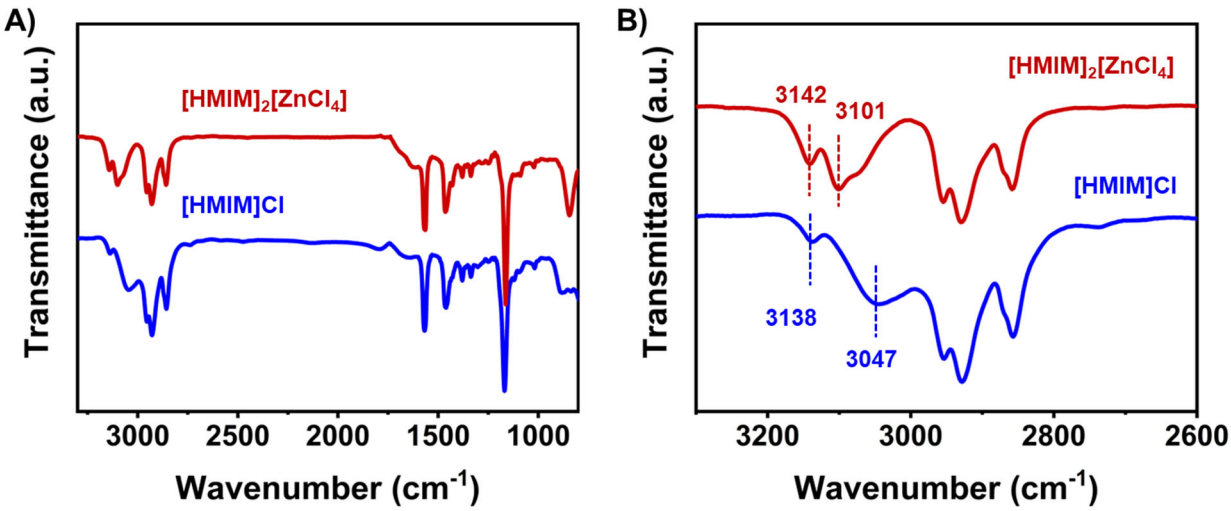

Fig. S2 (A) FT-IR spectra of [HMIM]Cl and $[HMIM]_2[ZnCl_4]$. (B) Magnified spectral region of C-H on imidazolium cation. The peaks at 3047 and 3138 cm^{-1}, corresponding to the stretching vibration band of C-H on the imidazolium cation, shifted to higher wavenumbers (3101 and 3142 cm^{-1}) after coordinating with metal ions.

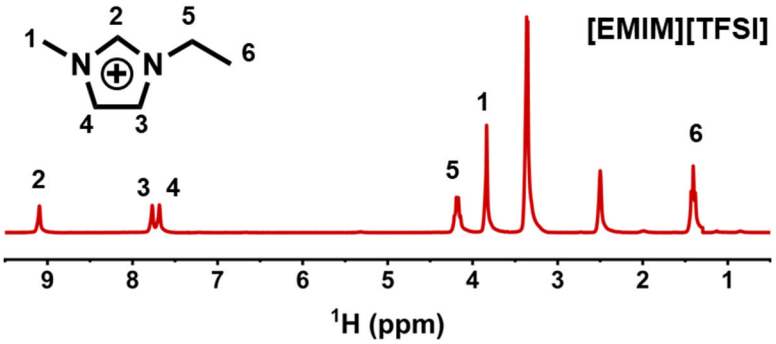

Fig. S3 ^1H NMR spectrum of [EMIM][TFSI].

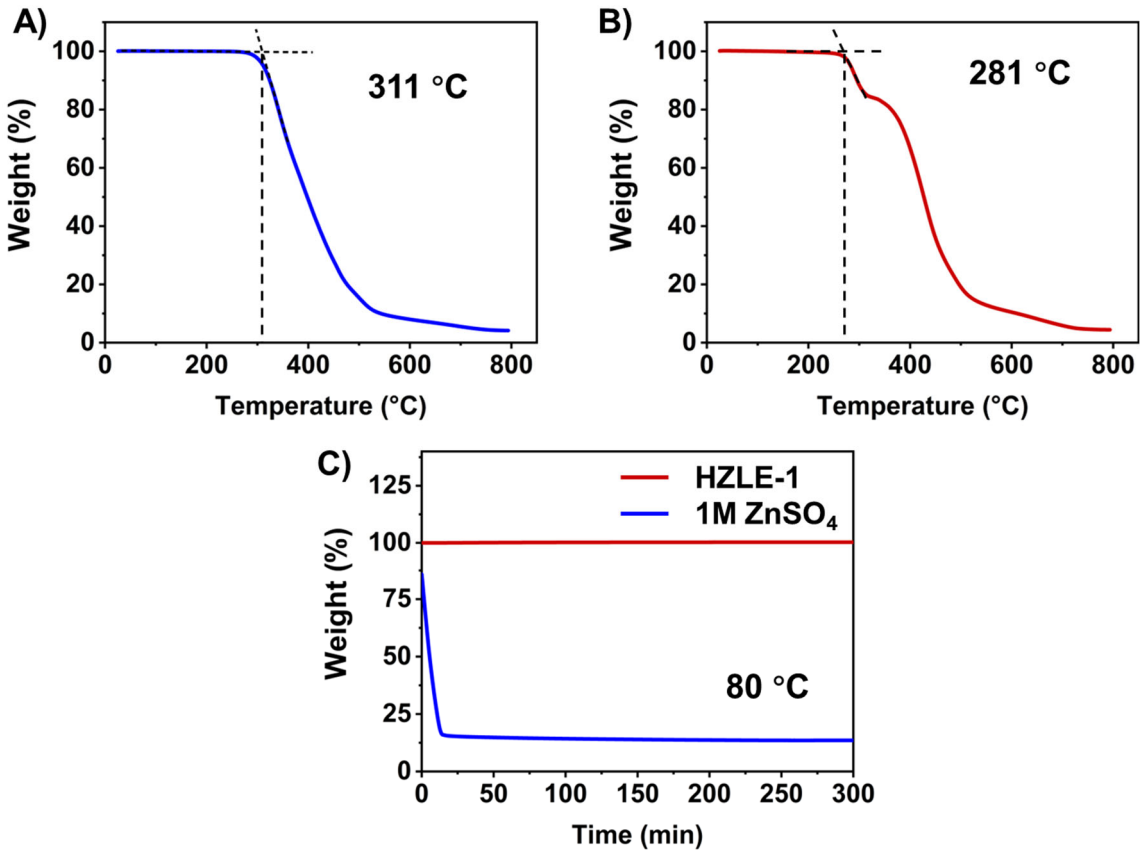

Fig. S4 Thermal decomposition curves of (A) $[HMIM]_2[ZnCl_4]$ and (B) HZLE-1 from 30 to 800 °C in N_2 (heating rate: 10 °C min^{-1}). (C) Thermal stability of the HZLE-1 and 1M $ZnSO_4$ electrolyte. The electrolytes were heated at 80 °C for 5 h in N_2 atmosphere. The HZLE-1 exhibits high thermal stability without weight loss while the water in 1M $ZnSO_4$ is volatilized resulting in rapid weight loss.

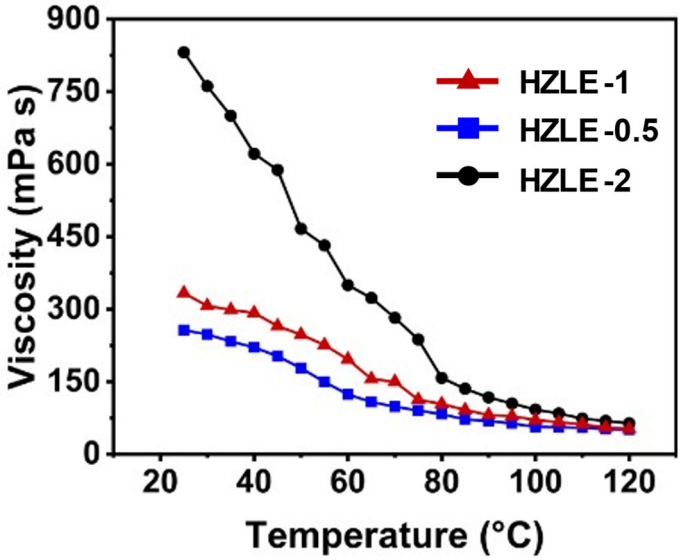

Fig. S5 Viscosity of HZLE-1, HZLE-0.5, and HZLE-2 from 25 to 120 °C.

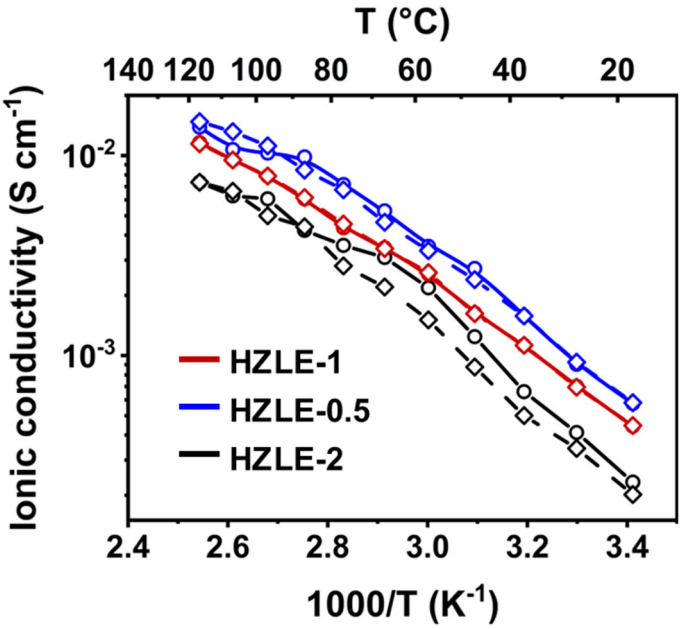

Fig. S6 Arrhenius plots of the overall ionic conductivities of HZLE-1 compared with HZLE-0.5 and HZLE-2. The hysteresis loops for three electrolytes during the measurement cycle with a heating course (solid lines, from 20 to 120 °C), then a cooling course (dashed lines, from 120 to 20 °C). Each temperature was maintained for 5 h.

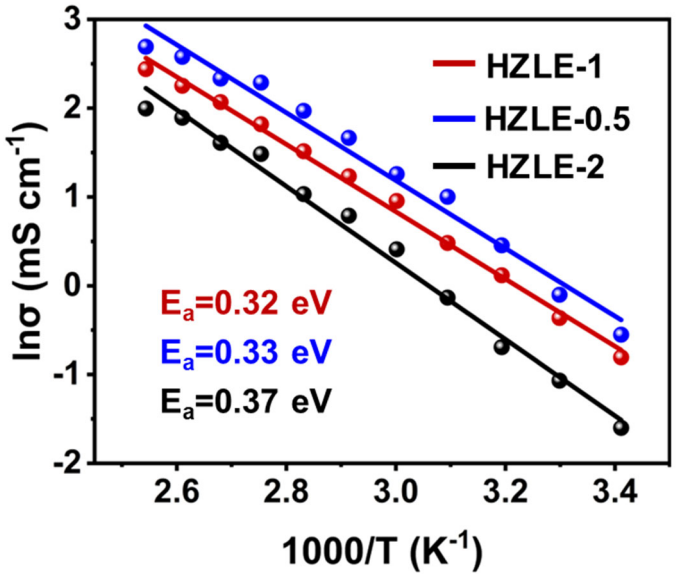

Fig. S7 Activation energies of ionic conductivities of HZLE-1, HZLE-0.5, and HZLE-2.

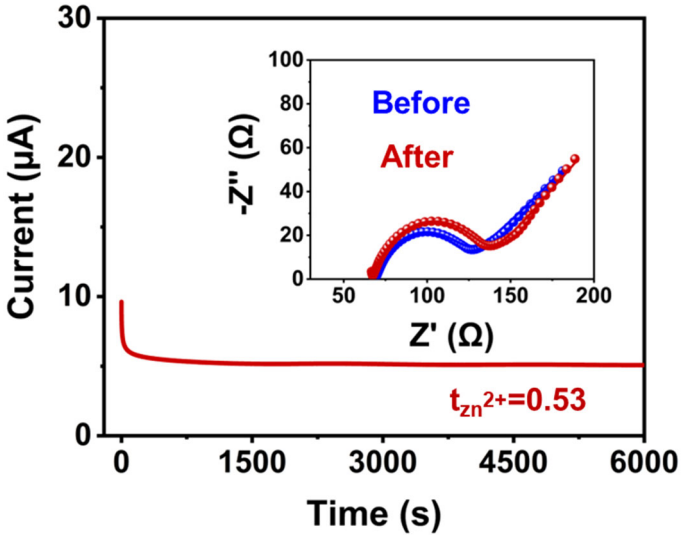

Fig. S8 Polarization curve and insert showed the Nyquist plots and fitting results before and after polarization of the Zn||Zn symmetric cell at 25 °C. Related parameters are presented in **Tables S1 and S2**.

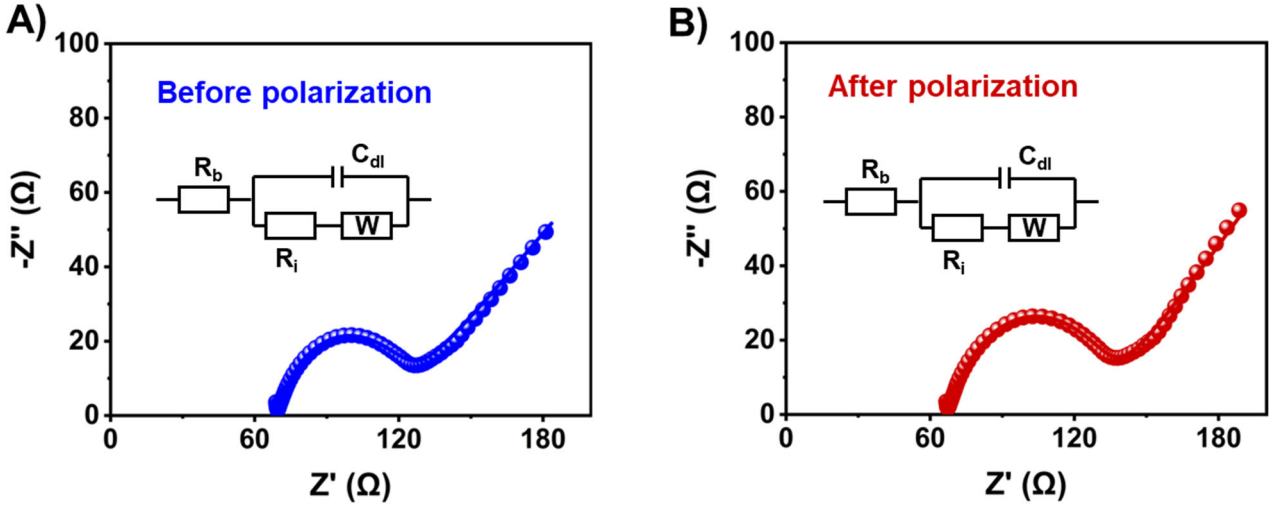

Fig. S9 Nyquist plots and fitting results (A) before and (B) after polarization of the Zn||Zn symmetric cell at 25 °C. Insert shows the equivalent circuit diagrams.

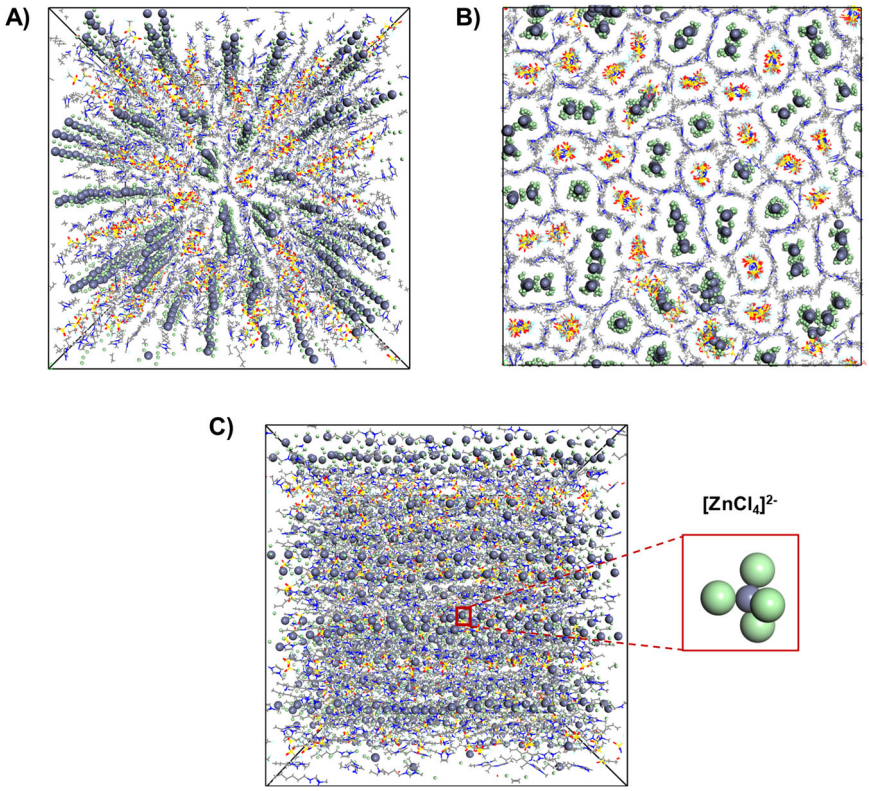

Fig. S10 (A) Three-dimensional, (B) two-dimensional snapshots, and (C) the Zn^{2+} presences of $[ZnCl_4]^{2-}$ state from MD simulation with the electric field (EF) in the HZLE-1 system (1.4 V).

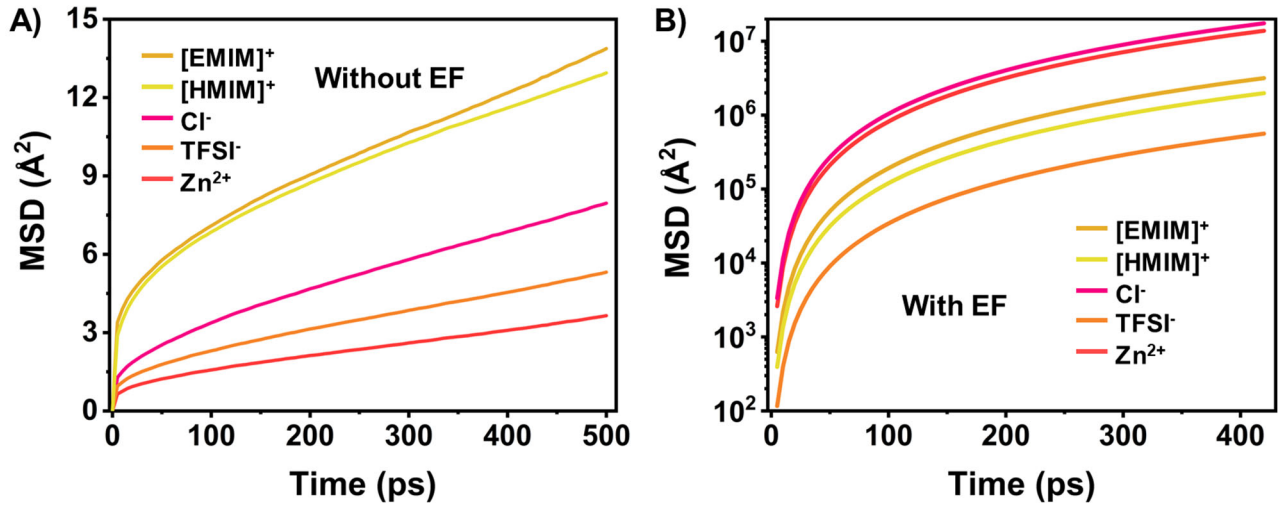

Fig. S11 Mean square displacement (MSD) of Zn^{2+}, Cl^{-}, $TFSI^{-}$, $[EMIM]^{+}$, and $[HMIM]^{+}$ of the HZLE-1 system (A) without electric field (without EF) and (B) with electric field (with EF, 1.4 V).

The interval of 100-500 ps was selected for the calculation of the diffusivity based on the MSD-t curve, and the results of the diffusivity obtained through Equation S4 are displayed in **Fig. 1H**:

$$Diffusivity \approx \frac{dMSD(t)}{6dt} = \frac{MSD(t)}{6t} \quad \text{(S4)}$$

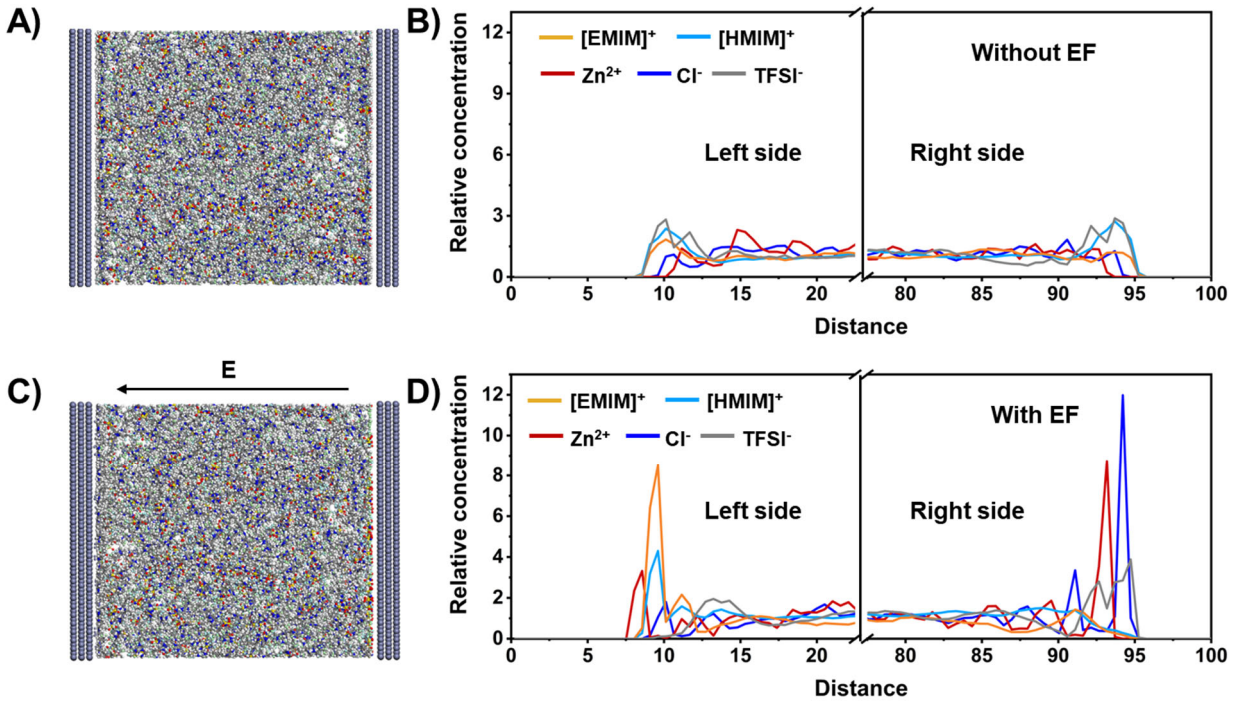

Fig. S12 Snapshots of the distribution of the ions on Zn electrodes (A) without EF and (C) with EF. Relative concentrations of the molecular numbers along the *z*-axis normal to the surface of Zn electrodes (B) without EF and (D) with EF (bias potential of 0.5 V).

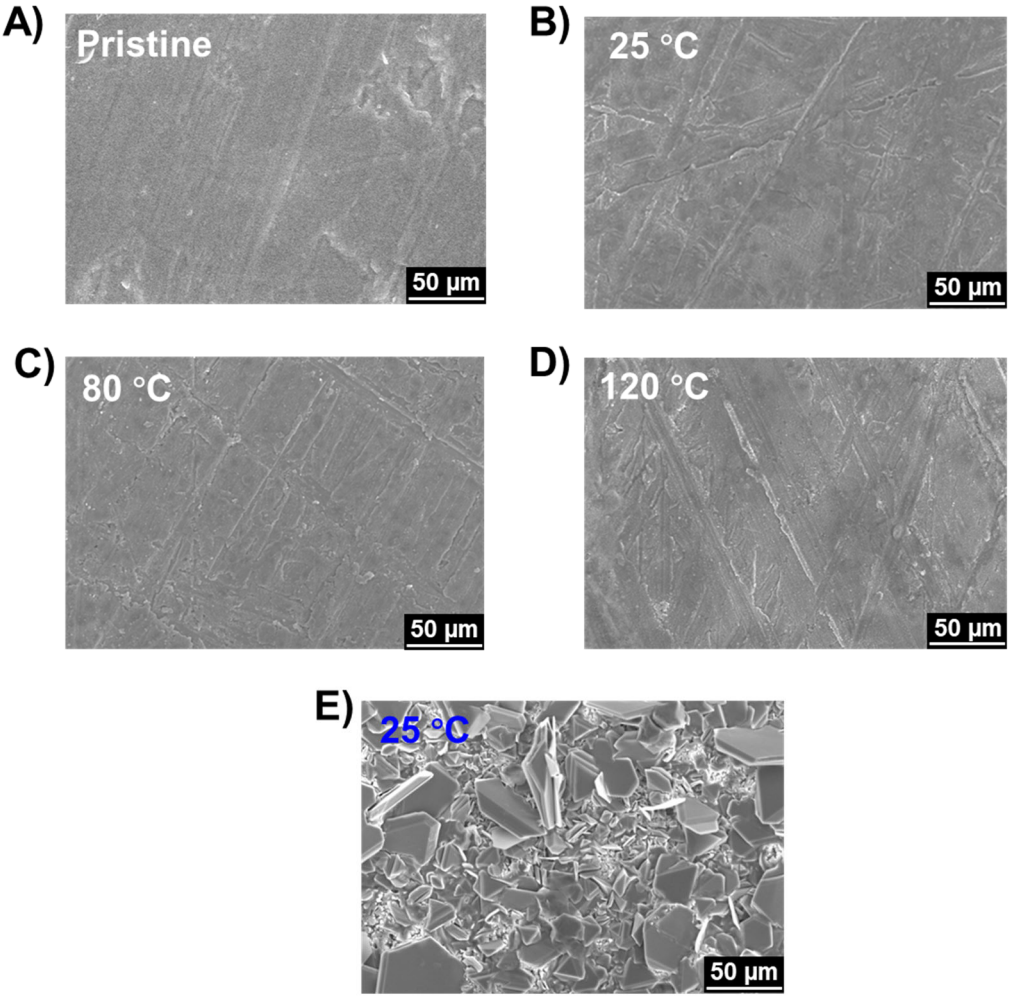

Fig. S13 (A) SEM images of pristine Zn foil. The SEM images of the Zn metal anode after immersion in HZLE-1 for 72 h at (B) 25 °C, (C) 80 °C, and (D) 120 °C and (E) after immersion in 1M $ZnSO_4$ for 72 h at 25 °C.

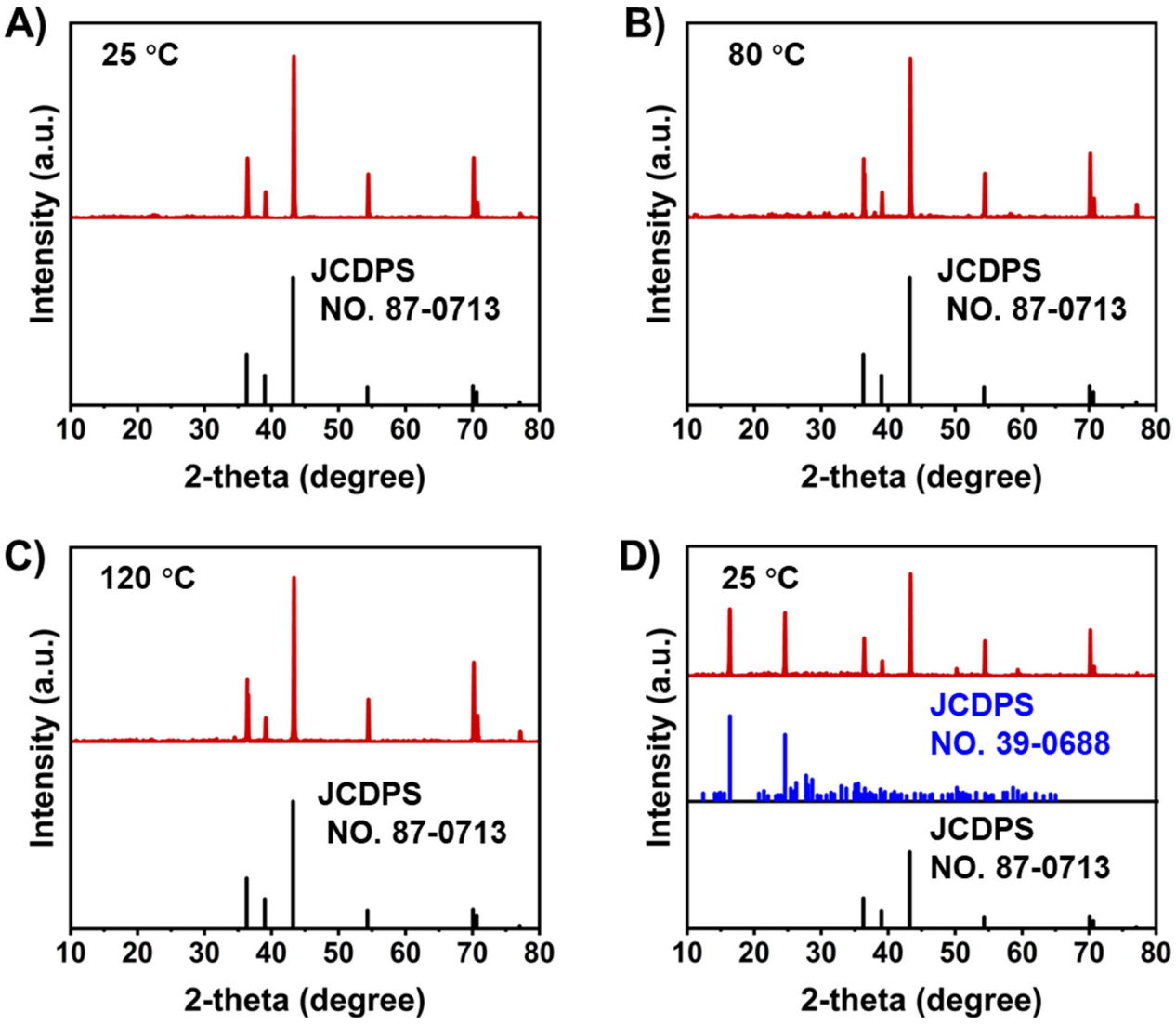

Fig. S14 XRD patterns of Zn metal anode after immersion in HZLE-1 for 72 h at (A) 25 °C, (B) 80 °C, and (C) 120 °C and (D) immersion in 1M $ZnSO_4$ for 72 h at 25 °C.

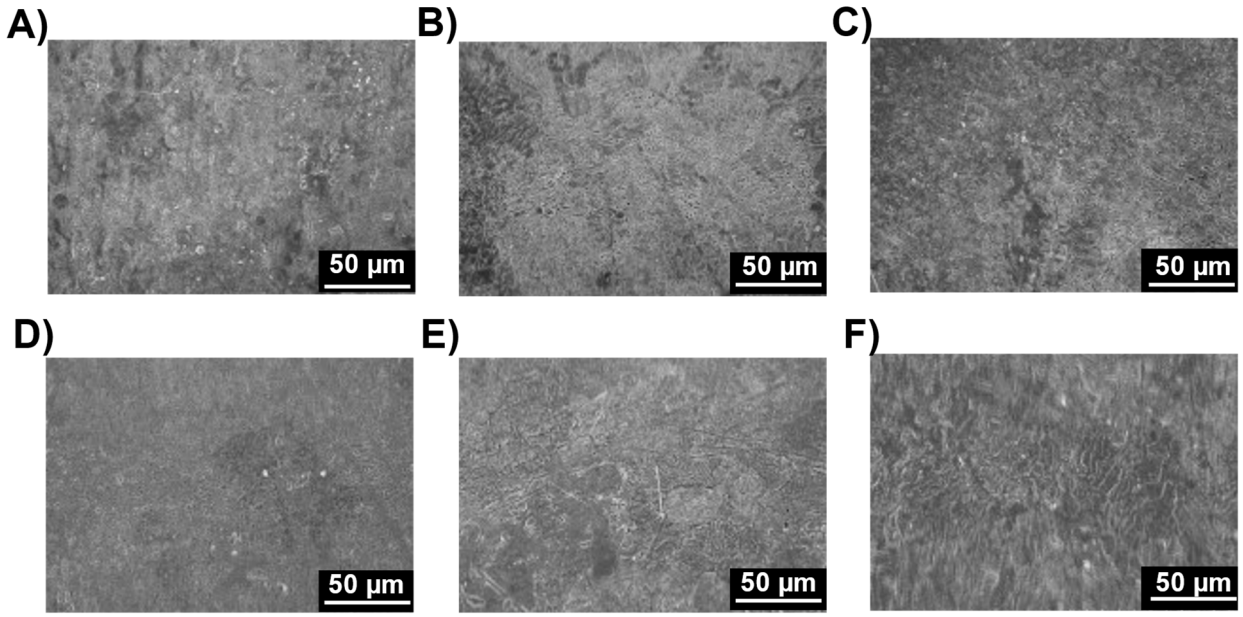

Fig. S15 SEM images of Zn foil after 10 cycles of Zn||Zn symmetric cells in HZLE-1 with an areal capacity of 6.25 mAh cm^{-2} (depth of discharge (DOD)=50%) at a current density of 0.2 mA cm^{-2} under (A) 25 °C, (B) 80 °C and (C) 120 °C. Images of Zn foil after 10 cycles in HZLE-1 with an areal capacity of 10 mAh cm^{-2} (DOD=80%) at a current density of 1 mA cm^{-2} under (D) 25 °C, (E) 80 °C and (F) 120 °C.

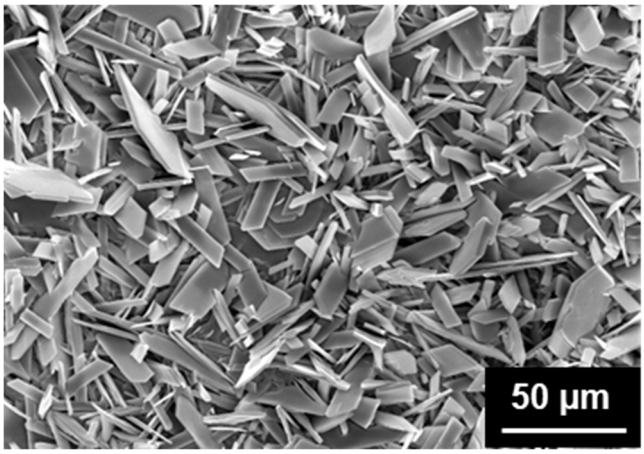

Fig. S16 SEM image of Zn metal anode after 10 cycles of a Zn||Zn symmetric cell in an electrolyte of 1 M $ZnSO_4$ under 25 °C with an areal capacity of 1.25 mAh cm^{-2} (DOD=10%) at a current density of 0.2 mA cm^{-2}.

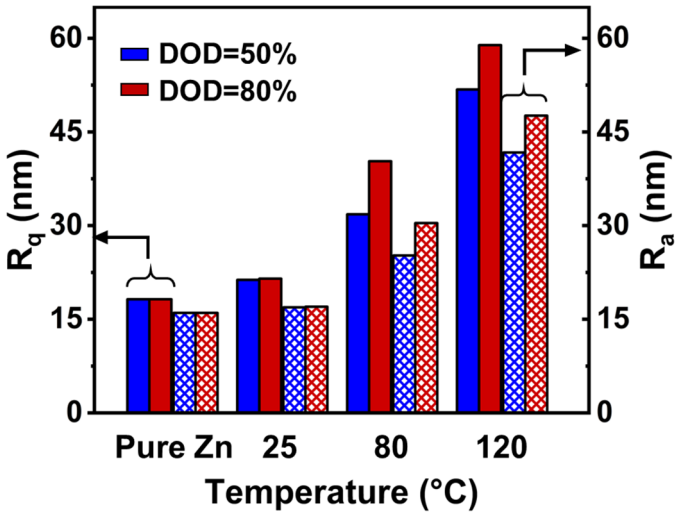

Fig. S17 R_q and R_a of Zn deposits obtained with different DODs of 50% and 80% varying temperature from 25 to 120 °C.

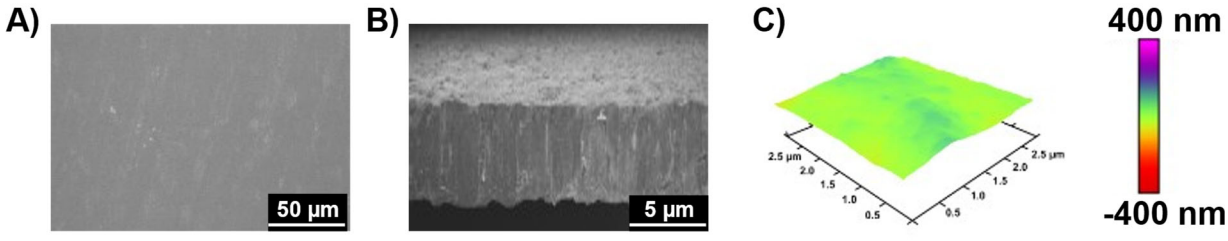

Fig. S18 (A) Typical SEM image, (B) cross-sectional SEM image, and (C) 3D morphology image of the pristine Zn.

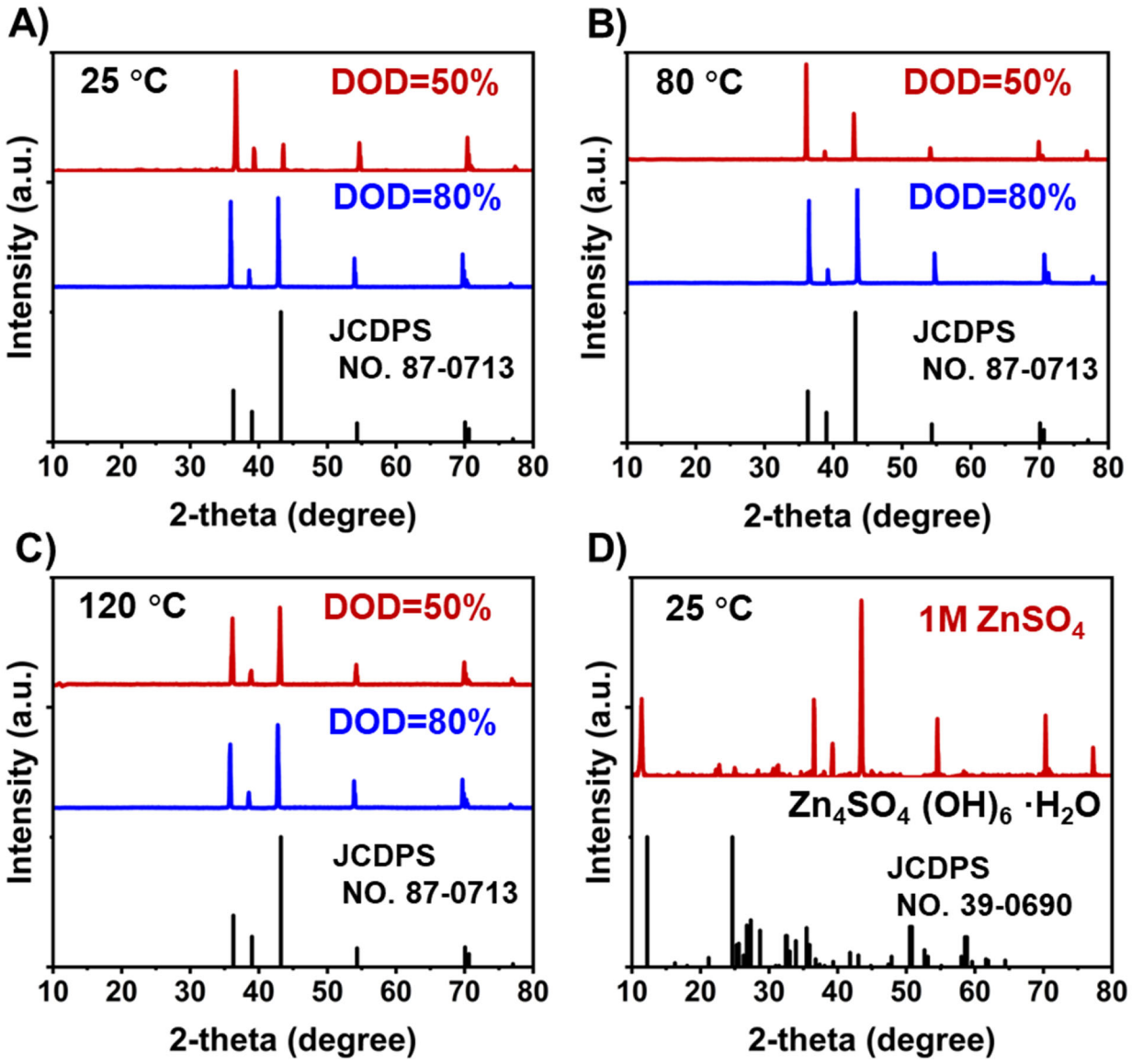

Fig. S19 XRD patterns of Zn deposits with different DODs after 10 cycles of Zn||Zn symmetric cells with HZLE-1 at (A) 25 °C, (B) 80 °C, (C)120 °C. (D) XRD pattern of Zn deposits with 0.2 mA cm^{-2}, 10% DOD after 10 cycles of Zn||Zn symmetric cell with 1M $ZnSO_4$ aqueous electrolyte at 25 °C.

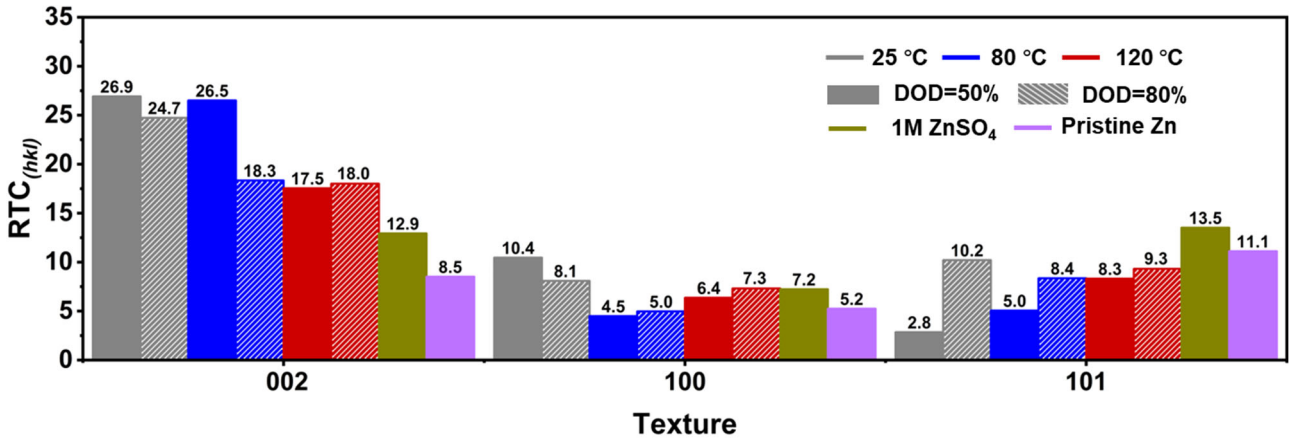

Fig. S20 $RTC_{(hkl)}$ of Zn deposits in HZLE-1, $ZnSO_4$ aqueous electrolyte, and pristine Zn without cycling obtained from **Fig. 3H** and **S19**.

Subsequently, the relative texture coefficients (*RTCs*) of each Zn lattice plane were calculated using Equation S5:

$$RCT_{(hkl)} = \frac{I_{(hkl)}/I_{0(hkl)}}{\sum\left(I_{(hkl)}/I_{0(hkl)}\right)} \times 100 \quad \text{(S5)}$$

where $I_{(hkl)}$ is the intensity obtained from the textured sample, and $I_{0(hkl)}$ is the intensity of the standard oriented sample (**Table S3**).

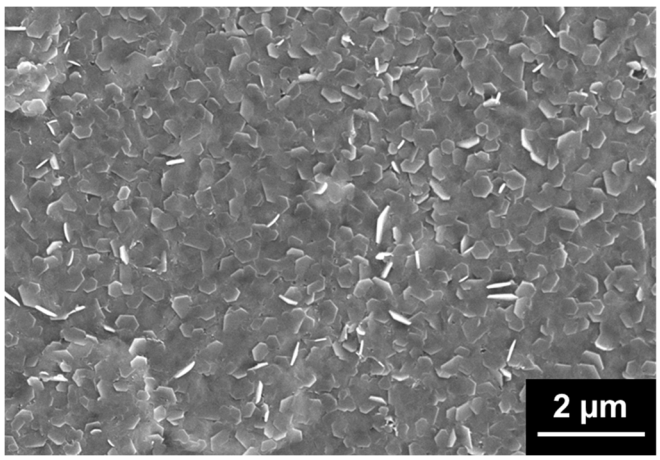

Fig. S21 SEM image of Zn metal anode after 10 cycles in HZLE-1 under 120 °C with DOD of 80% at a current density of 1 mA cm^{-2}.

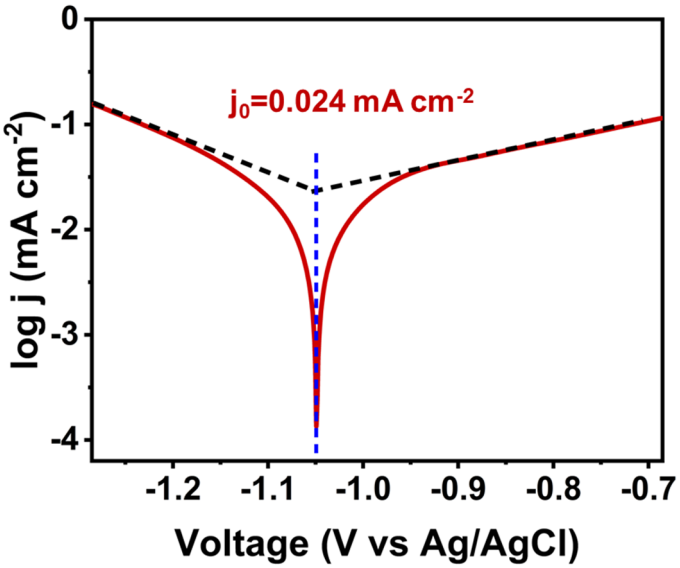

Fig. S22 Exchange current density (j_0) for Zn plating/stripping was calculated based on Tafel analysis, which involved using a Zn plate as the working and counter electrode (thickness of Zn plate: 50 μm), Ag/AgCl as the reference electrode, and conducting the analysis at a scan rate of 0.1 mV s^{-1}. Tafel plot was generated by plotting the overpotential of Zn plating/stripping against the log of the current density in the CV curve. The calculation of j_0 was determined by extracting the slope from the linear fitting of the overpotential to the applied current.

The kinetics of Zn^{2+} electroreduction are quantified as the faradaic current density j using the Butler-Volmer Equation S6 presented below:

$$j=j_0\left[e^{-\alpha nf\eta}-e^{(1-\alpha)nf\eta}\right] \quad \text{(S6)}$$

where j_0 is the exchange current density, α is the transfer coefficient, n is the number of electrons transferred, and η is the overpotential. Experimental interrogation of reaction kinetics is enabled through the relationship between measured values of j and η. Tafel plot analysis was executed to track the change in log j as η varied to obtain j_0 by extrapolating the measured j to the equilibrium state.

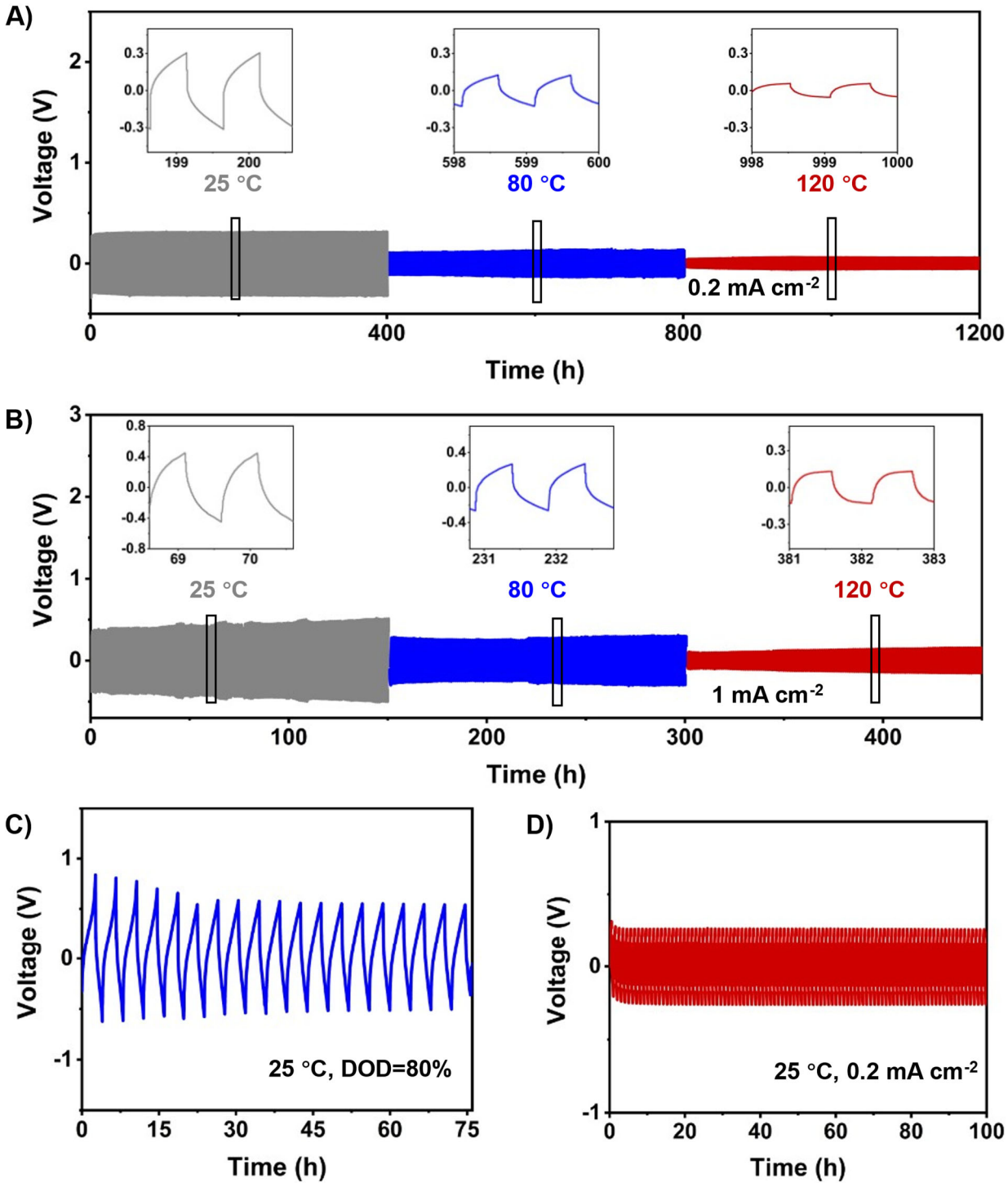

Fig. S23 Cycling stability of the Zn||Zn symmetric cell using HZLE-1 was evaluated over a temperature range from 25 to 120 °C under various current densities and areal capacities. (A) 0.2 mA cm^{-2} with an areal capacity of 0.2 mAh cm^{-2}, (B) 1 mA cm^{-2} with an areal capacity of 1 mAh cm^{-2}. Cycling performance of Zn||Zn symmetric cell with a current density of (C) 5 mA cm^{-2} and an areal capacity of 10 mA cm^{-2} at 25 °C (DOD=80%), (D) 0.2 mA cm^{-2} and an areal capacity of 0.2 mAh cm^{-2} at 25 °C with 30 µL electrolyte.

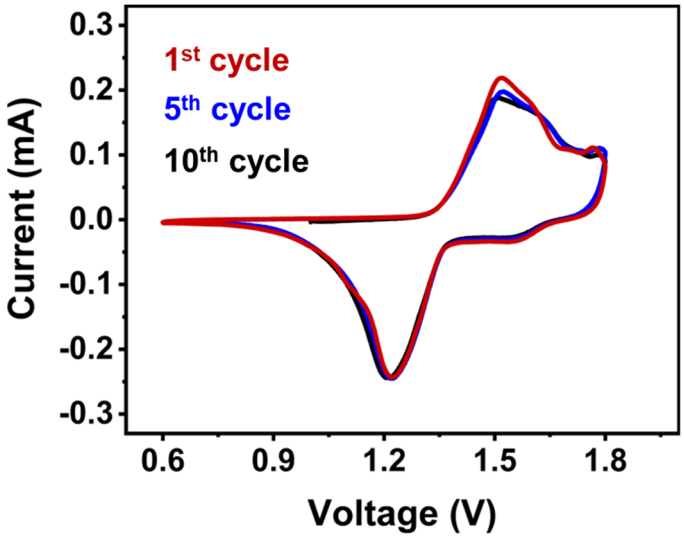

Fig. S24 CV curves of NVP||Zn cell with HZLE-1 at 0.1 mV s^{-1} for different cycles at 80 °C. The pair of oxidation/reduction peaks of V^{3+}/V^{4+} at around 1.45/1.21 V during the Zn^{2+} insertion/extraction process in NVP.

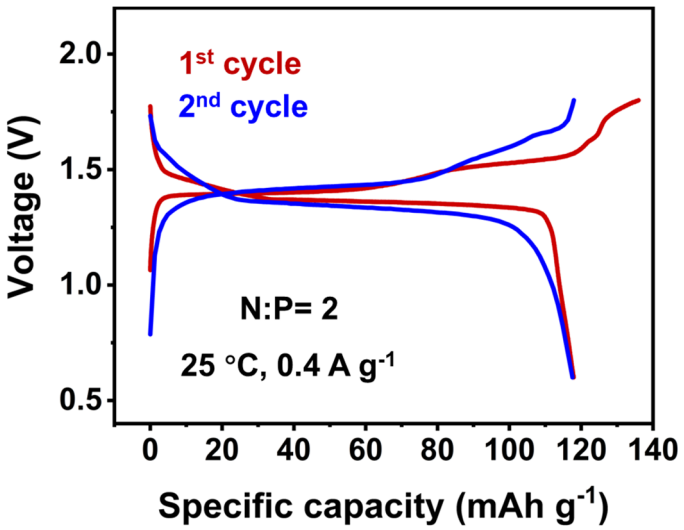

Fig. S25 Charge/discharge profiles of NVP||Zn cell with HZLE-1 at the first cycle and second cycle with a current density of 0.4 A g^{-1} and N:P ratio of 2 at 25 °C.

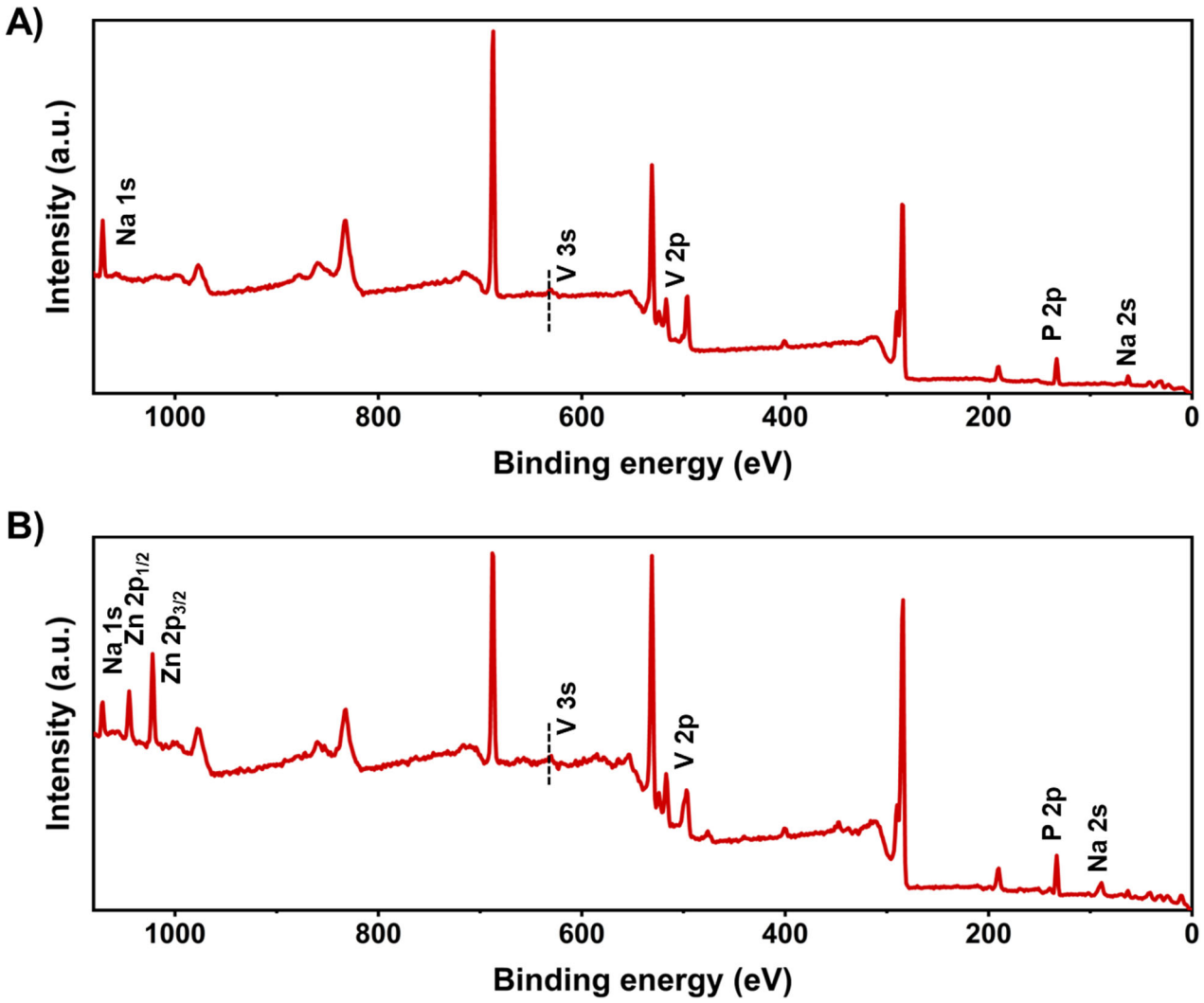

Fig. S26 Full-scan XPS spectra of (A) pristine NVP cathode without cycling and (B) NVP cathode after discharging to 0.6 V.

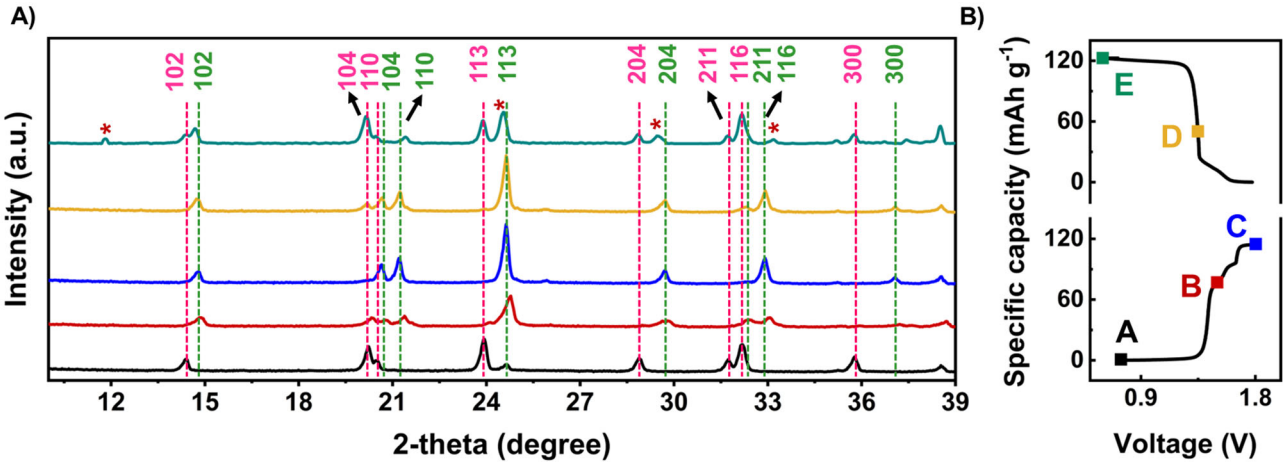

Fig. S27 (A) Ex-situ XRD patterns of NVP cathode. (B) GCD curve of the full cell for the first cycle at 0.4 A g^{-1}. Points A–E marked the states where data were collected for XRD analysis. From point A to C, the peaks associated with $Na_3V_2(PO_4)_3$ (dash pink) gradually decreased, while those related to $NaV_2(PO_4)_3$ (dash green) emerged. And the discharging process from point C to E, additional peaks at around 12.2°, 24.4°, 29.4°, and 33.2° appeared, indicating the formation of $Na_xZn_{1.5-0.5x}V_2(PO_4)_3$ ($0<x<3$) due to Zn^{2+} insertion into the $Na_3V_2(PO_4)_3$ phase.

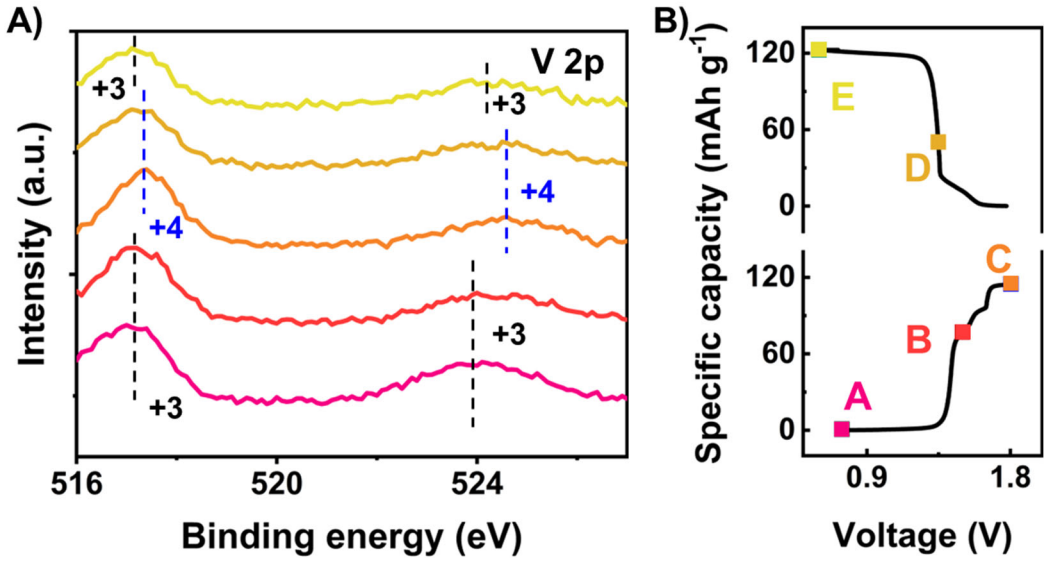

Fig. S28 (A) Ex-situ XPS spectra of NVP cathode at different discharged and charged states. (B) Corresponding GCD curve of the NVP||Zn cell for the first cycle at 0.4 A g^{-1}. Points A-E marked the states where data were collected for XPS analysis.

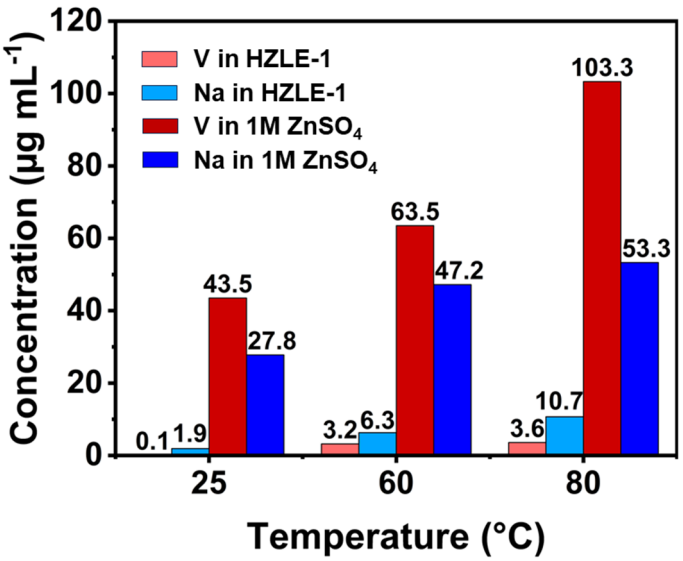

Fig. S29 Concentrations of vanadium (V) and sodium (Na) in the HZLE-1 after 10 cycles of NVP||Zn cell at 25 °C, 60 °C, and 80 °C and in the 1M $ZnSO_4$ electrolyte after 10 cycles of NVP||Zn cell at 25 °C, 60 °C. The concentrations of V and Na in the 1M $ZnSO_4$ electrolyte were investigated after 3 cycles of NVP||Zn cell at 80 °C, as a consequence of the cell failure that occurred after 3 cycles.

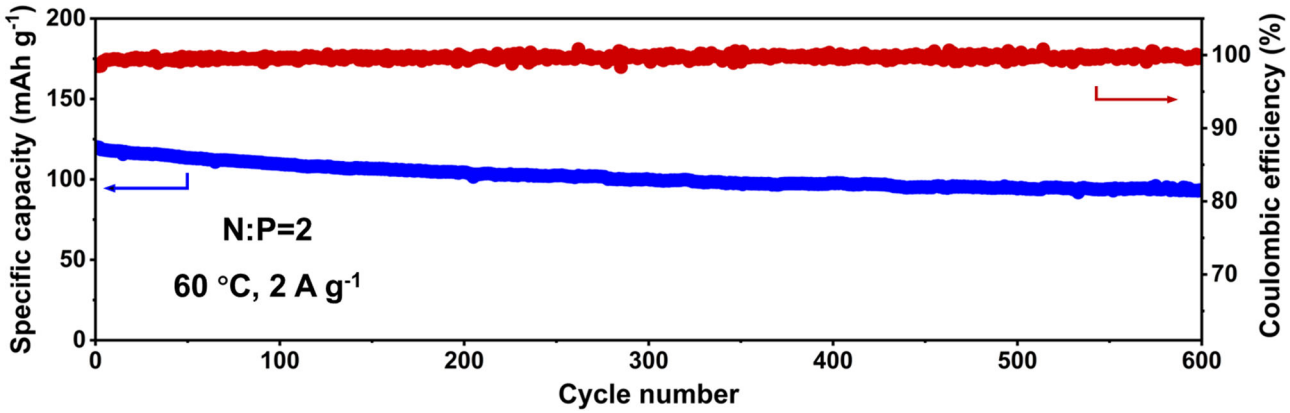

Fig. S30 Long-term stability of the NVP||Zn cell at 2 A g^{-1} under 60 °C. The N:P ratio is 2.

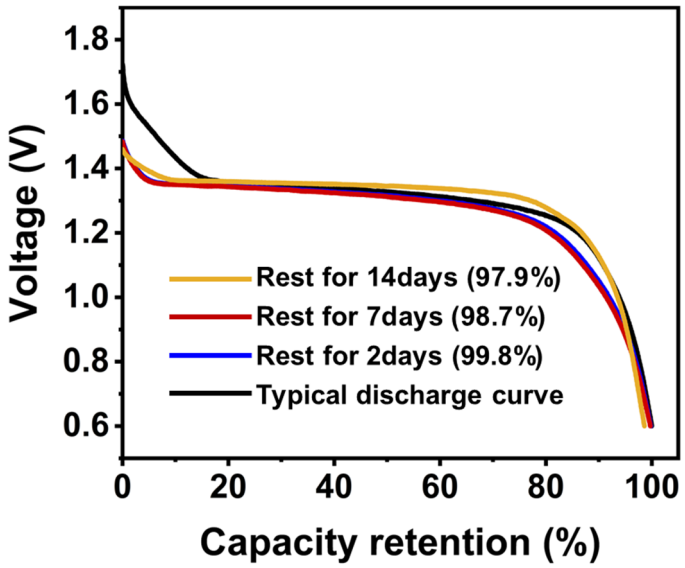

Fig. S31 Self-discharge performance of NVP||Zn cell with HZLE-1, which was measured at 80 °C with a current density of 2 A g^{-1}.

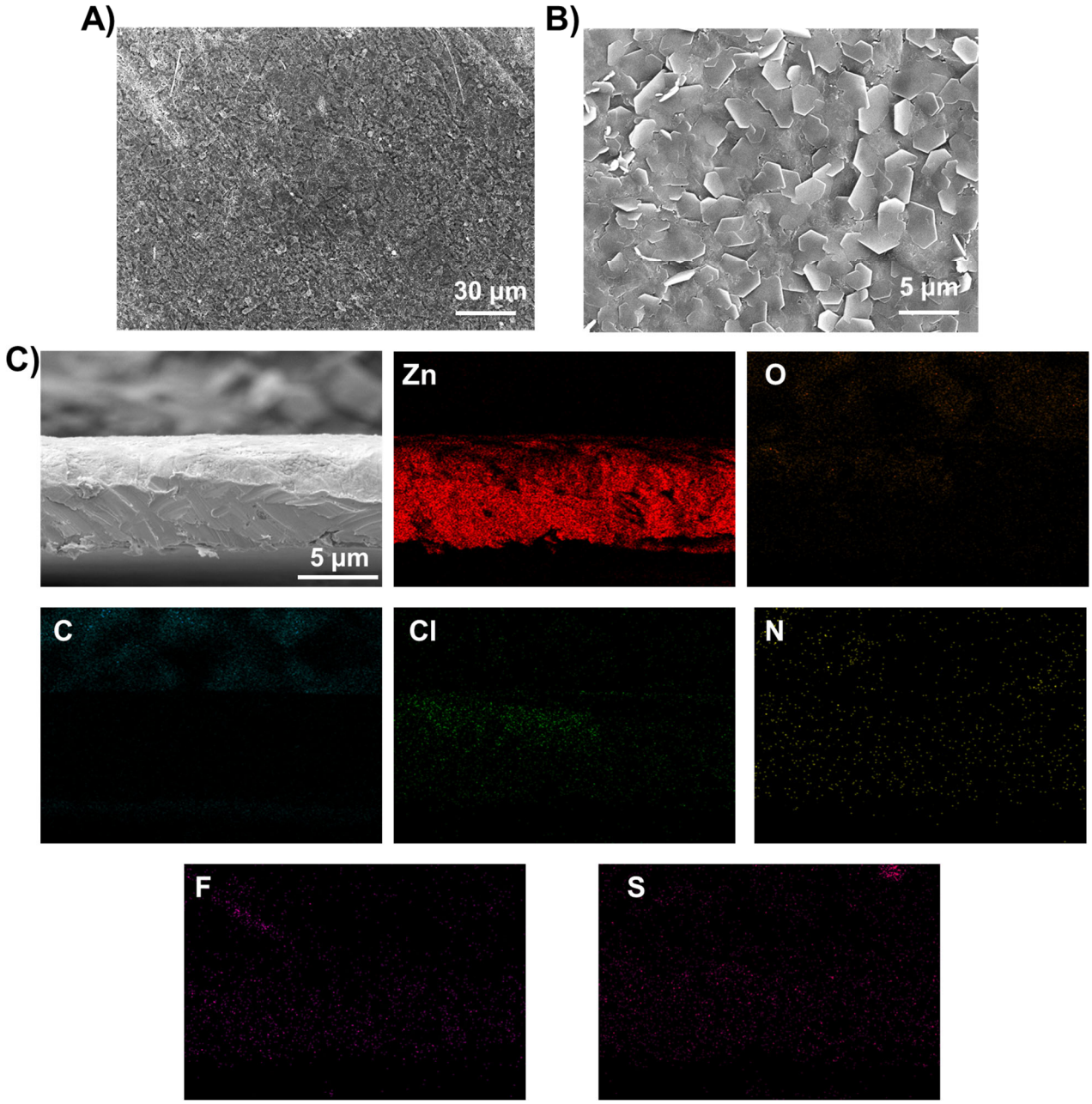

Fig. S32 SEM images of the surface region of the Zn anode cycled with HZLE-1 in the NVP||Zn full cell at 25 °C with (A) the scale bar of 30 μm, and (B) 5 μm. (C) SEM cross-sectional image of Zn metal anode after cycles of NVP||Zn cell with HZLE-1 at 25 °C and its corresponding EDS mappings. The distribution of Zn was observed without other elements distributed on the cross-section of the Zn anode.

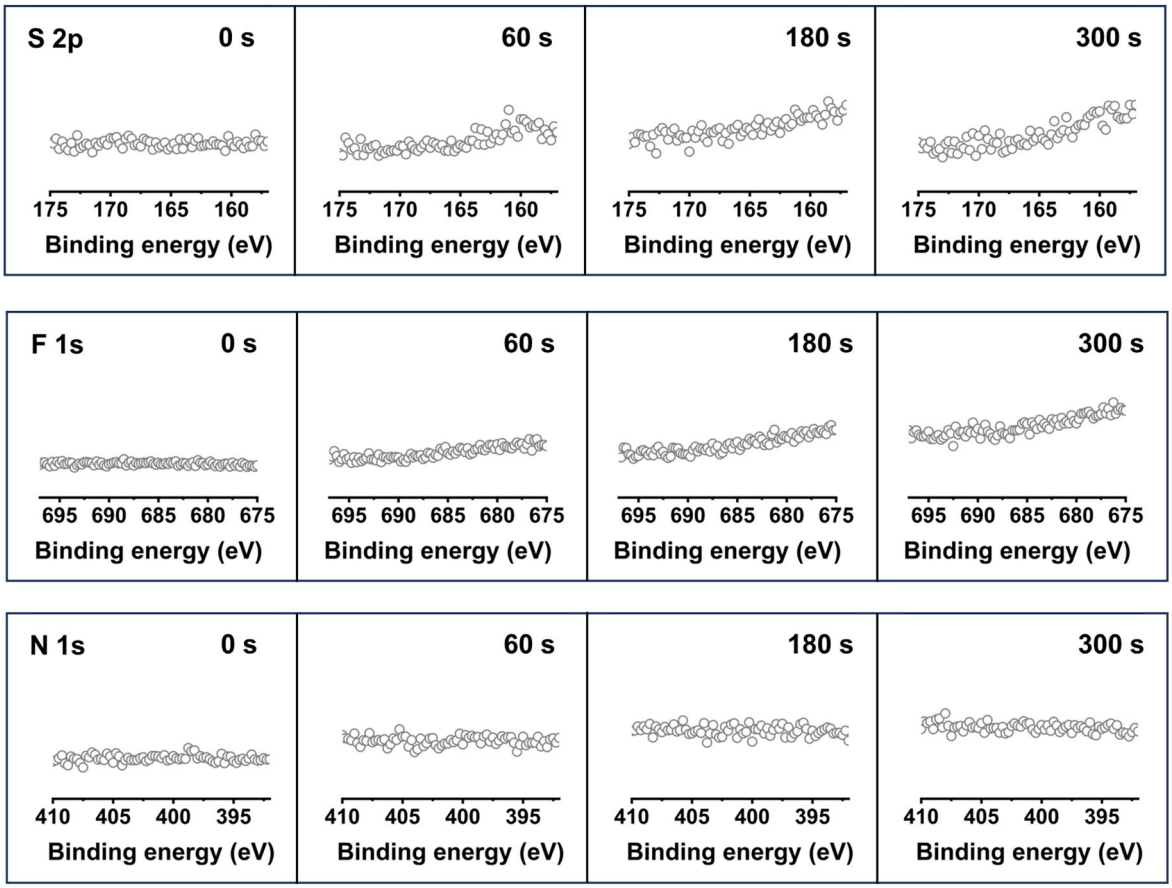

Fig. S33 XPS spectra with depth profiles of S 2p, F 1s, and N 1s of the Zn anode in NVP||Zn cell at 25 °C with 1000 cycles.

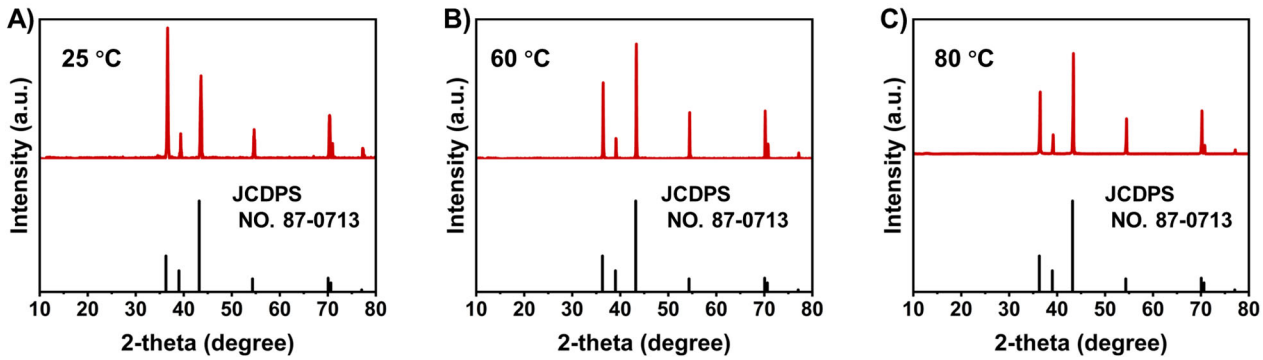

Fig. S34 XRD patterns of Zn anode after 50 cycles with HZLE-1 in the NVP||Zn full cell at (A) 25 °C, (B) 60 °C, and (C) 80 °C.

Fig. S35 Photos of the recyclability of HZLE-1. [HMIM]Cl was dissolved in water, while [EMIM][TFSI] was insoluble in water and $Zn_4(OH)_8Cl_2·H_2O$ was precipitated in water. Thus, [EMIM][TFSI] was separated by liquid-liquid phase separation and the $Zn_4(OH)_8Cl_2·H_2O$ and [HMIM]Cl were obtained by filtration.

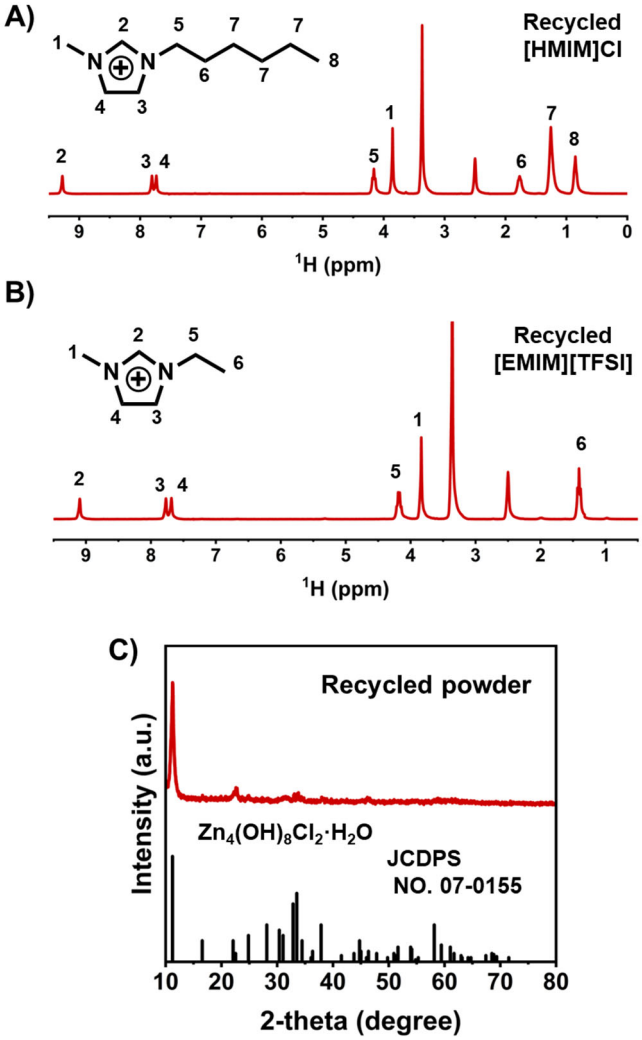

Fig. S36 ^{1}H NMR spectra of (A) recycled [HMIM]Cl, (B) recycled [EMIM][TFSI]. (C) XRD pattern of recycled $Zn_4(OH)_8Cl_2·H_2O$.

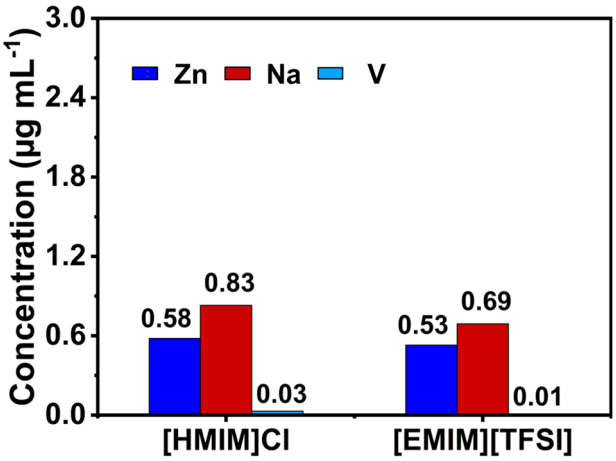

Fig. S37 Concentrations of Zn, Na, V in recycled [HMIM]Cl and recycled [EMIM][TFSI].

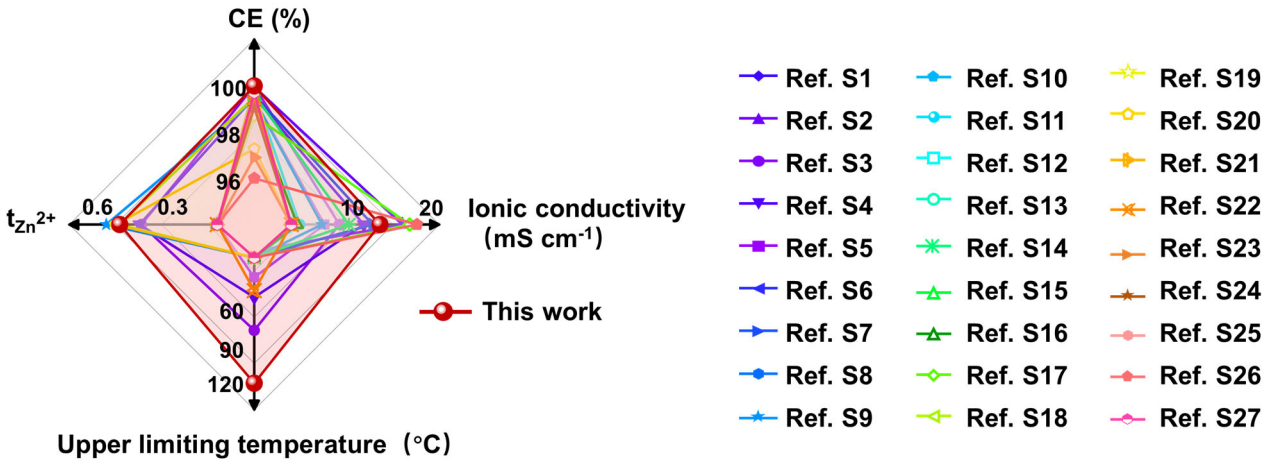

Fig. S38 Comprehensive comparison of the CE, ionic conductivity, upper limiting temperature, and tZn^{2+} for our work to the other reported literature.

Table S1 Fitting results of the equivalent circuit diagrams before and after polarization of the Zn||Zn symmetric cell at 25 °C.

	R_b (Ω)	R_i (Ω)
Before polarization	67.73	47.61
After polarization	64.52	59.40

Table S2 Parameters measured by d.c. polarization and EIS for calculating the t_{Zn}^{2+}.

	I^0 (μA)	I^{ss} (μA)	R_i^0 (Ω)	R_i^{ss} (Ω)	t_{Zn}^{2+}
HZLE-1	9.62	5.11	47.61	59.40	0.53

Table S3 Intensities obtained from textured samples $I_{(hkl)}$ under different conditions and the intensities of the standard oriented sample $I_{(hkl)}$ of Zn anodes.

Texture	**002**	**100**	**101**	**102**	**103**	**110**	**004**	
I_0	39.6	23.3	100	14.4	15.2	10	2.3	JCPDS NO. 87-0713
	2632	601	701	744	887	259	27	25 °C, DOD=50%
	21547	4145	22442	7175	8237	1688	106	25 °C, DOD=80%
	18654	1854	8968	2240	3483	2915	1061	80 °C, DOD=50%
I_{HZLE-1}	6079	968	6995	2199	2114	737	476	80 °C, DOD=80%
	12595	2686	15065	3846	4311	2149	1069	120 °C, DOD=50%
	12714	3037	16599	5145	5634	1624	637	120 °C, DOD=80%
I_0	53	40	100	28	25	21	2	JCPDS NO. 04-0831
	9684	4085	19102	5145	5417	1646	919	Pristine Zn
I	516	240	1271	420	405	70	103	25 °C, DOD=10% 1 M $ZnSO_4$

Table S4 Atomic percentage (%) of each element in the pristine cathode of NVP and the NVP after charging at 0.6 V obtained by XPS spectra.

Atom (%)	Na	Zn	V	P	Chemical formula
Pristine	3.82	0	2.51	3.7	$Na_3V_2(PO_4)_3$
After charging	0.85	1.35	2.3	3.52	$Na_{0.73}Zn_{1.17}V_2(PO_4)_3$

The quantitative analysis of XPS is based on the fact that the intensity of the photoelectron spectral lines (the area of the photoelectron peaks) reflects the atomic content. Therefore, by integrating the peaks of the xps spectrum, the changes in the elemental content of the NVP before and after charging were obtained. And the theoretical capacity was calculated by Equation S7:

$$C=\frac{nF}{3.6M}\ \left(\text{mAh g}^{-1}\right) \tag{S7}$$

where n represents the number of electrons involved in the electrochemical reaction, F is Faraday's constant (96485 C mol^{-1}), and M is the molar mass of the active substance.

Table S5 Recovery rates and mass of [HMIM]Cl and [EMIM][TFSI] by extraction for multi-component separation.

	$m_{pristine}$ (g)	$m_{recycled}$ (g)	Recovery rate
[HMIM]Cl	2.02	1.88	93%
[EMIM][TFSI]	1.96	1.86	95%

The reaction equation for hydrolysis is

$$4[HMIM]_2[ZnCl_4]+4[EMIM][TFSI]+8ZnCl_2+27H_2O$$

$$\rightarrow 8[HMIM]Cl+4[EMIM][TFSI]+3Zn_4(OH)_8Cl_2\cdot H_2O+18HCl+6H^+$$

Table S6. Comparison of the Coulombic efficiency, ionic conductivities, upper limiting temperature, and t_{Zn}^{2+} of reported literature developed for high-performance Zn metal batteries.[S1–S27]

	Coulombic efficiency (%)	**Ionic conductivity (mS cm^{-1})**	**Upper limiting temperature (°C)**	**t_{Zn}^{2+}**
This work	**99.99%**	**12**	**120**	**0.53**
Nature Sustainability 2022, 5, 205–213	99.40%	4.5	40	N.A.
Nature Sustainability 2023, 6, 325–335	99.99%	6.5	80	0.41
Nature Sustainability 2023, 6, 806–815	99.95%	15	20	N.A.
Nature Sustainability 2023, 6, 1474–1484	99.50%	9.8	55	0.421
Nature Materials 17, 2018, 543–549	99.70%	N.A.	25	N.A.
Energy Environ. Sci., 2023, 16, 2540-2549	99.60%	11	25	N.A.
Energy Environ. Sci., 2023, 17, 717-726	98.04%	N.A.	25	N.A.
Energy Environ. Sci., 2024, 17, 3443-3453	99.39%	4.15	25	0.6
Angew. Chem.Int. Ed. 2022, 61, e202206717	99.70%	1.15	25	N.A.
Angew. Chem.Int. Ed. 2022, 61, e202211589	98.50%	N.A.	25	N.A.
Angew. Chem.Int. Ed. 2022, 61, e202212780	99.57%	N.A.	25	N.A.
Angew. Chem.Int. Ed. 2024, 63, e202316499	99.60%	7.8	25	N.A.
Angew. Chem.Int. Ed.2023, 62, e202302174	99.57%	N.A.	25	N.A.
Angew. Chem.Int. Ed. 2024, 63, e202318496	99%	0.79	25	N.A.
Angew. Chem.Int. Ed. 2023, 62, e202307880	98.70%	16	25	N.A.
Angew. Chem.Int. Ed. 2023, 62, e202302302	99.50%	N.A.	25	0.53
Angew. Chem.Int. Ed. 2024, 63, e202402206	99.90%	N.A.	25	N.A.
Angew. Chem.Int. Ed. 2024, 63, e202319051	97.27%	N.A.	25	0.55
Angew. Chem.Int. Ed. 2024, 63, e202403050	99.51%	N.A.	50	N.A.
J. Am. Chem. Soc. 2023, 145, 22456–22465	99.50%	N.A.	55	N.A.
J. Am. Chem. Soc. 2024, 146, 9455−9464	99.55%	6	25	N.A.
Joule 2022, 6, 1103–1120	99.80%	N.A.	25	N.A.
Adv.Mater.2022, 34, 2206963	96.90%	N.A.	25	N.A.
Adv.Mater.2022, 34, 2207344	99.06%	N.A.	25	N.A.
Adv. Mater.2023,35, 2210055	99.70%	N.A.	25	N.A.
Adv.Mater.2023, 35, 2207131	96%	17	25	N.A.
Adv. Mater.2024,36, 2306145	99.70%	N.A.	25	N.A.

Movie S1

An MD simulated process of Zn^{2+} transport in the HZLE-1 system with electric field.

Movie S2

NVP||Zn pouch cell powered an electronic timer at 80 °C.

Supplementary references

S1. D. Han, C. Cui, K. Zhang, Z. Wang, J. Gao, Y. Guo, Z. Zhang, S. Wu, L. Yin, Z. Weng, F. Kang and Q. H. Yang, *Nat. Sustain.*, 2022, **5**, 205–213.

S2. C. Yang, J. Xia, C. Cui, T. P. Pollard, J. Vatamanu, A. Faraone, J. A. Dura, M. Tyagi, A. Kattan, E. Thimsen, J. Xu, W. Song, E. Hu, X. Ji, S. Hou, X. Zhang, M. S. Ding, S. Hwang, D. Su, Y. Ren, X. Q. Yang, H. Wang, O. Borodin and C. Wang, *Nat. Sustain.*, 2023, **6**, 325–335.

S3. H. Jiang, L. Tang, Y. Fu, S. Wang, S. K. Sandstrom, A. M. Scida, G. Li, D. Hoang, J. J. Hong, N. C. Chiu, K. C. Stylianou, W. F. Stickle, D. Wang, J. Li, P. A. Greaney, C. Fang and X. Ji, *Nat. Sustain.*, 2023, **6**, 806–815.

S4. D. Dong, T. Wang, Y. Sun, J. Fan and Y. C. Lu, *Nat. Sustain.*, 2023, **6**, 1474–1484.

S5. F. Wang, O. Borodin, T. Gao, X. Fan, W. Sun, F. Han, A. Faraone, J. A. Dura, K. Xu and C. Wang, *Nat. Mater.*, 2018, **17**, 543–549.

S6. R. Chen, C. Zhang, J. Li, Z. Du, F. Guo, W. Zhang, Y. Dai, W. Zong, X. Gao, J. Zhu, Y. Zhao, X. Wang and G. He, *Energy Environ. Sci.*, 2023, **16**, 2540–2549.

S7. L. Zhi, C. Liao, P. Xu, F. Sun, C. Yuan, F. Fan, G. Li, Z. Yuan and X. Li, *Energy Environ. Sci.*, 2023, **17**, 717–726.

S8. Z. Yang, Y. Sun, S. Deng, H. Tong, M. Wu, X. Nie, Y. Su, G. He, Y. Zhang, J. Li and G. Chai, *Energy Environ. Sci.*, 2024, **17**, 3443–3453.

S9. L. Geng, J. Meng, X. Wang, C. Han, K. Han, Z. Xiao, M. Huang, P. Xu, L. Zhang, L. Zhou and L. Mai, *Angew. Chemie - Int. Ed.*, 2022, **61**, e202206717.

S10. M. Kim, S. J. Shin, J. Lee, Y. Park, Y. Kim, H. Kim and J. W. Choi, *Angew. Chemie - Int.*

Ed., 2022, **61**, e202211589.

S11. B. Liu, C. Wei, Z. Zhu, Y. Fang, Z. Bian, X. Lei, Y. Zhou, C. Tang, Y. Qian and G. Wang, *Angew. Chemie - Int. Ed.*, 2022, **61**, e202212780.

S12. W. Deng, Z. Deng, Y. Chen, R. Feng and X. Wang, *Angew. Chemie - Int. Ed.*, 2024, **63**, e202316499.

S13. B. Raza, Y. Zhang, J. Chen, U. Shamraiz, Y. Zhang, A. Naveed and J. Wang, *Angew. Chemie - Int. Ed.*, 2023, **62**, e202302174.

S14. F. Bu, Y. Gao, W. Zhao, Q. Cao, Y. Deng, J. Chen, J. Pu, J. Yang, Y. Wang, N. Yang, T. Meng, X. Liu and C. Guan, *Angew. Chemie - Int. Ed.*, 2024, **63**, e202318496.

S15. L. Zhou, R. Yang, S. Xu, X. Lei, Y. Zheng, J. Wen, F. Zhang and Y. Tang, *Angew. Chemie - Int. Ed.*, 2023, **62**, e202307880.

S16. J. Luo, L. Xu, Y. Zhou, T. Yan, Y. Shao, D. Yang, L. Zhang, Z. Xia, T. Wang, L. Zhang, T. Cheng and Y. Shao, *Angew. Chemie - Int. Ed.*, 2023, **62**, e202302302.

S17. Z. Wu, Y. Li, A. Amardeep, Y. Shao, Y. Zhang, J. Zou, L. Wang, J. Xu, D. Kasprzak, E. Hansen and J. Liu, *Angew. Chemie Int. Ed.*, 2024, **63**, e202402206.

S18. Q. Wu, J. Huang, J. Zhang, S. Yang, Y. Li, F. Luo, Y. You, Y. Li, H. Xie and Y. Chen, *Angew. Chemie - Int. Ed.*, 2024, **63**, e202319051.

S19. S. Zhou, X. Meng, Y. Chen, J. Li, S. Lin, C. Han, X. Ji, Z. Chang and A. Pan, *Angew. Chemie - Int. Ed.*, 2024, **63**, e202403050.

S20. W. Xu, J. Li, X. Liao, L. Zhang, X. Zhang, C. Liu, K. Amine, K. Zhao and J. Lu, *J. Am. Chem. Soc.*, 2023, **145**, 22456–22465.

S21. K. Zhou, G. Liu, X. Yu, Z. Li and Y. Wang, *J. Am. Chem. Soc.*, 2024, **146**, 9455–9464.

S22. C. Li, A. Shyamsunder, A. G. Hoane, D. M. Long, C. Y. Kwok, P. G. Kotula, K. R. Zavadil, A. A. Gewirth and L. F. Nazar, *Joule*, 2022, **6**, 1103–1120.

S23. J. Hao, L. Yuan, Y. Zhu, M. Jaroniec and S. Z. Qiao, *Adv. Mater.*, 2022, **34**, 2206963.

S24. Q. Ma, R. Gao, Y. Liu, H. Dou, Y. Zheng, T. Or, L. Yang, Q. Li, Q. Cu, R. Feng, Z. Zhang, Y. Nie, B. Ren, D. Luo, X. Wang, A. Yu and Z. Chen, *Adv. Mater.*, 2022, **34**, 2207344.

S25. H. Du, Y. Dong, Q. J. Li, R. Zhao, X. Qi, W. H. Kan, L. Suo, L. Qie, J. Li and Y. Huang, *Adv. Mater.*, 2023, **35**, 2210055.

S26. P. Chen, X. Sun, T. Pietsch, B. Plietker, E. Brunner and M. Ruck, *Adv. Mater.*, 2023, 35, 2207131.

S27. C. Wang, J. Z. J. Zhu, S. Vi-Tang, B. Peng, C. Ni, Q. Li, X. Chang, A. Huang, Z. Yang, E. J. Savage, S. Uemura, Y. Katsuyama, M. F. El-Kady and R. B. Kaner, *Adv. Mater.*, 2024, **36**, 2306145.